



MSU Graduate Theses

Fall 2017


A Study of Manganese and Cobalt Incorporated Nickel Oxide Based Core-Shell Magnetic Nanoparticles

Samiul Hasan

Missouri State University, Samiul097@live.missouristate.edu

As with any intellectual project, the content and views expressed in this thesis may be considered objectionable by some readers. However, this student-scholar's work has been judged to have academic value by the student's thesis committee members trained in the discipline. The content and views expressed in this thesis are those of the student-scholar and are not endorsed by Missouri State University, its Graduate College, or its employees.

Follow this and additional works at: <https://bearworks.missouristate.edu/theses>

 Part of the [Nanoscience and Nanotechnology Commons](#), and the [Other Materials Science and Engineering Commons](#)

Recommended Citation

Hasan, Samiul, "A Study of Manganese and Cobalt Incorporated Nickel Oxide Based Core-Shell Magnetic Nanoparticles" (2017). *MSU Graduate Theses*. 3208.
<https://bearworks.missouristate.edu/theses/3208>

This article or document was made available through BearWorks, the institutional repository of Missouri State University. The work contained in it may be protected by copyright and require permission of the copyright holder for reuse or redistribution.

For more information, please contact bearworks@missouristate.edu.

**A STUDY OF MANGANESE AND COBALT INCORPORATED NICKEL OXIDE
BASED CORE-SHELL MAGNETIC NANOPARTICLES**

A Master's Thesis

Presented to

The Graduate College of
Missouri State University

In Partial Fulfillment

Of the Requirements for the Degree
Masters of Science, Materials Science

By

Samiul Hasan

December 2017

Copyright 2017 by Samiul Hasan

A STUDY OF MANGANESE AND COBALT INCORPORATED NICKEL OXIDE BASED CORE-SHELL MAGNETIC NANOPARTICLES

Physics, Astronomy and Materials Science

Missouri State University, December 2017

Master of Science

Samiul Hasan

ABSTRACT

The synthesis along with the structural and magnetic properties of manganese (Mn) and cobalt (Co) -incorporated nickel oxide (NiO) inverted core-shell nanoparticles (CSNs) were investigated. The primary objective of this study was to determine the effect of substitution of nickel (Ni) by transition metal ions (Mn^{2+}/Co^{2+}) in affecting the magnetic properties of the resultant CSNs. The core of the CSNs is comprised of NiO and the shell constitutes a $Ni_x(Mn/Co)_{1-x}O$ phase. The synthesis of the CSNs was accomplished in two steps: first, NiO nanoparticles were synthesized using a thermal decomposition method. In the second step, our hydrothermal nanophase epitaxy method was used to create the core-shell structure. Rietveld refinement of X-ray diffraction (XRD) data show rock salt structure throughout in the Mn/Co incorporated CSNs. Scanning electron microscopy (SEM) and transmission electron microscopy (TEM) images show a combination of pseudo-spherical and faceted shapes of CSNs whereas energy dispersive spectroscopy (EDS) indicates transition metal incorporation in the CSNs. The high-resolution (HR) TEM images confirmed the formation of distinct core and shell regions. Magnetic characterization shows that the Mn- and Co-substituted nickel oxide-based CSNs possess an inverted magnetic structure, with an antiferromagnetic core and a ferro- or ferrimagnetic shell. The coercivity and exchange bias properties are of larger magnitude in Mn-incorporated than in Co-incorporated CSNs.

KEYWORDS: core-shell nanoparticles, magnetic, exchange bias, hysteresis, coercivity

This abstract is approved as to form and content

Robert A. Mayanovic, PhD
Chairperson, Advisory Committee
Missouri State University

**A STUDY OF MANGANESE AND COBALT INTRODUCED NICKEL OXIDE
BASED CORE-SHELL MAGNETIC NANOPARTICLES**

By

Samiul Hasan

A Master's Thesis
Submitted to the Graduate College
Of Missouri State University
In Partial Fulfillment of the Requirements
For the Degree of Master of Science, Materials Science

December 2017

Approved:

Robert A. Mayanovic, PhD

Ridwan Sakidja, PhD

Fei Wang, PhD

Julie Masterson, PhD: Dean, Graduate College

In the interest of academic freedom and the principle of free speech, approval of this thesis indicates the format is acceptable and meets the academic criteria for the discipline as determined by the faculty that constitute the thesis committee. The content and views expressed in this thesis are those of the student-scholar and are not endorsed by Missouri State University, its Graduate College, or its employees.

ACKNOWLEDGEMENTS

I would like to thank Dr. Robert A. Mayanovic for mentoring me for the last two years; guide me in my research, for hearing patiently my lots of illogical logics, teaching me patience in my impatient time. I wish I could get him as my supervisor in my future studies. I am thankful to Dr. Kartik Ghosh for his help in different instrumentation, Dr. Ridwan Sakidja for his computation and experimental suggestions and other faculties and Graduate students of PAMS. I am very grateful to Mr. Rishi Patel of Jordan Valley Innovation Center (JVIC) for his patient help with different measurements. I am also thankful to Dr. Mourad Benamara – Director, Institute of Nanoscience and Engineering at University of Arkansas, Fayetteville for his help with Transmission Electron Microscope (TEM) images. I am very thankful to the Department of Physics, Astronomy and Materials Science of Missouri State University for providing enormous facilities to complete my graduate studies here.

I dedicate this thesis to my loving wife Dr. Israt Jahan Manar

TABLE OF CONTENTS

Chapter 1: Introduction.....	1
Chapter 2: Synthesis and characterization of NiO@Ni _x Mn _{1-x} O core-shell nanoparticles	11
Abstract.....	11
Introduction.....	12
Experimental.....	13
Results and Discussion.....	15
Conclusion.....	26
References.....	26
Chapter 3: Investigation of novel inverted NiO@Ni _x Co _{1-x} O core-shell nanoparticles.....	28
Abstract.....	28
Introduction.....	29
Experimental.....	31
Results and Discussion.....	33
Conclusion.....	41
References.....	41
Chapter 4: Summary.....	44
References.....	46
Appendix : Additional Data.....	49

LIST OF TABLES

Table 2.1. Magnetic moment of individual atom in NiO and structure $\text{Ni}_{0.88}\text{Mn}_{0.12}\text{O}$ 25

Table 3.1. Magnetic moment of individual atom in NiO and structure $\text{Ni}_{0.88}\text{Co}_{0.12}\text{O}$ 40

LIST OF FIGURES

Figure 1.1: Schematic of the exchange bias (EB) phenomenon as a shift in the magnetic hysteresis loop at a low temperature when the sample is cooled in the presence of a magnetic field from a high temperature, well above the Néel or blocking temperature	4
Figure: 1.2 Schematic diagram of FM/AFM bilayer showing exchange bias effect. The grey layer has AFM spin structure, while the violet one represents FM layer. M-H hysteresis loop is shifted along the field axis demonstrating exchange bias at temperature $T < T_N$	6
Figure: 1.3 Schematic diagram of synthesized CSNs.....	8
Figure: 1.4 Summary of synthesis procedure	9
Figure 2.1. (a) SEM image of NiO@Ni _x Mn _{1-x} O and (b) corresponding EDX spectra.....	16
Figure 2.2. (a) Low resolution TEM image of NiO@Ni _x Mn _{1-x} O and (b) corresponding size distribution of particles	17
Figure 2.3: High resolution TEM image of NiO@Ni _x Mn _{1-x} O.....	17
Figure 2.4: Rietveld refinement profile of the powder XRD pattern of CSNs.....	19
Figure 2.5: (a) Zero field cooled (ZFC) and field cooled (FC) magnetization vs applied field (M vs H) measurement data for NiO@Ni _x Mn _{1-x} O CSNs (at 5 K temperature) for 0.05M Mn precursor concentration: The inset shows the data near the H = 0 Oe region, (b) Magnetization vs temperature data (range 5 K to 330 K).....	20
Figure 2.6: (a) Zero field cooled (ZFC) and field cooled (FC) magnetization vs applied field (M vs H) measurement data for NiO@Ni _x Mn _{1-x} O CSNs (at 5 K temperature) with 0.08M precursor concentration (b) Magnetization vs temperature data (range 5 K to 330 K)	22
Figure 2.7: Coercivity vs Temperature for 0.08M precursor used CSNs	23
Figure 2.8: Spin Orientation of supercell.....	24
Figure 2.9. DOS and partial DOS (pDOS) from our DFT-based calculations of NiO (left panels) and Ni _{0.88} Mn _{0.12} O (right panels)	24
Figure 3.1. (a) SEM image of NiO@Ni _x Co _{1-x} O and (b) corresponding EDX spectra	34
Figure 3.2. (a) Low resolution TEM image of NiO@Ni _x Co _{1-x} O and (b) corresponding size distribution of particles	34

Figure 3.3: High resolution TEM image of NiO@Ni _x Co _{1-x} O	35
Figure 3.4: Rietveld refinement profile of the powder XRD pattern of CSNs	36
Figure 3.5. (a) Zero field cooled (ZFC) and field cooled (FC) magnetization vs applied field (M vs H) measurement data for NiO@Ni _x Co _{1-x} O CSNs (at 5 K temperature): The inset shows the data near the H = 0 Oe region and positive and negative saturation. (b) Magnetization vs temperature data (range 5 K to 300 K).....	37
Figure 3.6. (a) ZFC hysteresis of Co ₃ O ₄ NPs, (b) ZFC hysteresis of NiO NPs (both at 5 K)	38
Figure 3.7. DOS and partial DOS (pDOS) from our DFT-based calculations of NiO (left panels) and Ni _{0.88} Co _{0.12} O (right panels)	40

CHAPTER 1: INTRODUCTION

Nanoscale materials are key to solving many major technological global problems related to energy harvesting and conversion, electronics, computation, communication, space exploration, medicinal applications, and biomedical engineering. Confinement in at least one or more spatial dimensions gives rise to the unique optical, magnetic, electric, thermal and mechanic properties. The tuning of physical/chemical properties through critical surface/interface studies of multifunctional composite core-shell nanostructures allow the possibility of combining distinct material functionalities into one overall structure [1-3]. In the growing research of nanostructured materials, magnetic nanoparticles (NP) and nano-composites are of substantial interest to researchers in academia and industry in recent years due to the large number of potential applications, including for catalytic, magnetic, electronic, and biomedical applications [4]. Different synthesis techniques have made it possible to prepare nanostructured materials with highly controlled and varying dimensions, which has helped to advance the field of nano-magnetism towards practical applications [5].

Core-shell nanoparticle (CSN) are presently of great interest in the field of nanomaterials. The core-shell structure can constitute different types based on composition, size, and shape of the NPs. Magnetic core-shell nanoparticles are classified based on possessing a magnetic component; bimagnetic CSNs possess both a magnetic core and a magnetic shell. Nanoparticles having a ferromagnetic (FM) or ferrimagnetic (FiM) core and an antiferromagnetic (AFM) shell are known as regular bimagnetic CSNs [6-10]. On the other hand, ones having an AFM core and a FM/FiM shell are known as

inverted bimagnetic core-shell nanoparticles. The interaction between core and shell can give rise to the exchange bias property [1]. The amount of experimental and theoretical work on core-shell exchange-coupled nanoparticles has increased recently. This is due to the unique property of bimagnetic core shell nanoparticles whereby tuning the structural and compositional properties of core and shell plays a significant role in shaping the overall magnetic and other physical/chemical characteristics of the CSNs.

The structural and morphological properties of the core shell nanoparticles mostly depend on the synthesis procedure. One of the first methods employed for synthesis of bimagnetic CSNs was oxidation of a transition metal NP at the surface to form an oxidized AFM shell (e.g., Ni/NiO) [11]. Although this method is comparatively less complicated, it offers less variety than more recent methods. There are numerous synthesis techniques that have been developed since metal NP oxidation, such as homogenous precipitation, co-precipitation, impregnation, sol-gel, sono-chemical, micro-emulsion, hydrothermal, and thermal decomposition methods [12]. In case of synthesis of bimagnetic core shell nanoparticles, it is important to have a well ordered interface region in between the core and shell to get desirable structure, and thereby, physicochemical (including magnetic) properties of the shell and at the surface of the CSNs. In most of the cases, the synthesis of CSNs is relatively inexpensive, but the alignment between synthesis methodology and desired properties of the CSNs needs to be approached with care. Special interest has been paid to the synthesis methods which yield nanoparticles with a narrow size distribution and controlled sizes or shapes [12].

Magnetic nanoparticles show different properties than the bulk materials of same composition due to the competition between finite size effect and collective effects of

inter-particle interaction [12]. Superparamagnetism is the direct consequence of finite size effect of the particles, which can create problems in magnetic memory application due to thermal destabilization of recording units. Conversely, the thermal destabilization is some time needed, such as for various biomedical applications. Meiklejohn and Bean were the first to report an exchange anisotropy (which is more commonly referred to today as the exchange bias effect) involving an interaction between the AFM Co core with the FM CoO shell leading to a preferential magnetization in one direction (i.e., uniaxial anisotropy) of Co/CoO CSNs [13]. Recently it has been reported that exchange interactions between an AFM core and a FM/FiM shell or vice versa can be used to overcome the superparamagnetic limit.

The exchange bias effect has been studied in much greater detail in thin bilayer thin film systems. This is because the planar, two dimensional geometry lends itself much more easily to both experimental and theoretical interrogation than the three dimensional geometry of nanoparticle systems. Nevertheless, the study of the exchange bias effect in bimagnetic CSNs is one of the growing areas in nanoparticle research. Although much is known about the exchange bias of CSNs, it is still under active investigation today. It is an interface phenomenon which arises due to spin coupling effect between a AFM-FM/FiM or FM/FiM-AFM interface [14]. The exchange bias (EB) effect is illustrated in the Figure 1.1. The EB effect can be observed experimentally by making magnetization vs applied magnetic field measurements in the field cooled (FC) and zero field cooled (ZFC) condition. Typically, the exchange bias effect is revealed in a hysteresis shift along the (negative) applied field direction and/or in a shift along the (positive) magnetization axis of the FC vs ZFC curve.

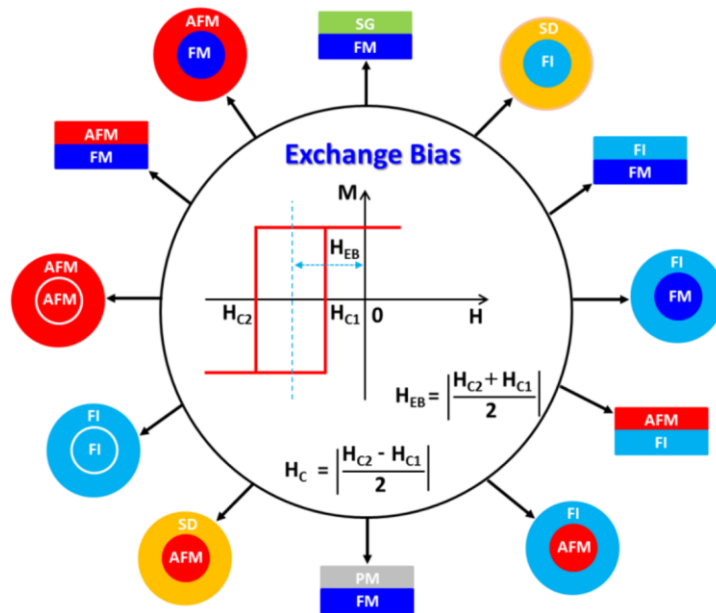


Figure 1.1: Schematic of the exchange bias (EB) phenomenon as a shift in the magnetic hysteresis loop at a low temperature when the sample is cooled in the presence of a magnetic field from a high temperature, well above the Néel or blocking temperature [15].

The EB effect has been reported in a wide range of magnetic systems with different types of interfaces involving FM, FI, AFM, SG, SD and PM magnetic phases, where the acronyms stand for ferromagnetic, ferrimagnetic, antiferromagnetic, spin-glass, spin disordered and paramagnetic, respectively [15].

When an interfaced system of AFM and FM/FiM material layer is cooled in the ZFC condition below the Néel temperature (T_N), the AFM spin pairs align randomly at the minimum energy configuration. If the external magnetic field (H) is varied, the spins at the interface in the FM/FiM layer align in the direction of applied field. Therefore, the ZFC case produces a hysteresis loop which is centered on both the magnetic field (H) and the magnetization (M) axes. When the same system is cooled, starting from the same temperature as the FC case, in the applied saturation magnetic field below T_N (the value

of applied field depends on the type of material), the surface spins of the AFM material couple with the FM/FiM surface spin due to the EB effect. The EB interaction induces parallel alignment of the uncompensated interface spins of the FM/FiM layer and the AFM layer. In the FC condition, the hysteresis loop undergoes a shift (which can be horizontal and/or only vertical or by an increase in the coercivity). The schematic diagram shown in Figure 1.2 serves to illustrate the EB effect of a FM/AFM bilayer. The grey layer has the AFM spin structure, while the violet one represents the spin structure of the FM layer. When the external field (\mathbf{H}) is driven in the negative direction and attempts to induce a torque in order to flip the spins of the FM/FiM layer, there is a cost in energy to do so that does not exist in the ZFC condition. Eventually, as \mathbf{H} is increased in the negative direction, the FM/FiM spins are flipped whereas the direction of the spins of the AFM layer remains unchanged. As a result, when \mathbf{H} is driven from negative to positive values (i.e., typically the “bottom” side of the hysteresis loop) and induces a torque to flip the direction of the spins in the FM/FiM layer, it takes less energy to do so due to the “positive” orientation of the interface spins in the AFM layer. Thus, the M-H hysteresis loop is shifted along the \mathbf{H} field axis illustrating the exchange bias at temperature $T < T_N$ in Figure 1.2. Because of the EB interaction, a number of FM/FiM spins remain aligned in the direction of AFM interface spins as \mathbf{H} is reduced to zero from $H > 0$. On the other hand, as \mathbf{H} approaches zero from the $H < 0$ side, there can be significantly fewer number of FM/FiM spins aligned in the opposite direction of the AFM interface spins. This accounts for the vertical shift along the M axis of the hysteresis loop. Although the exchange bias effect originates from uncompensated interface spins, it is also thought to depend upon surface/interface defects, oxygen

vacancy, frozen spins due to spin-order disorder, reduced coordination at facet/surface nanoparticle terminations and potentially other effects. These mostly depend on the synthesis technique and are therefore extremely difficult to control.

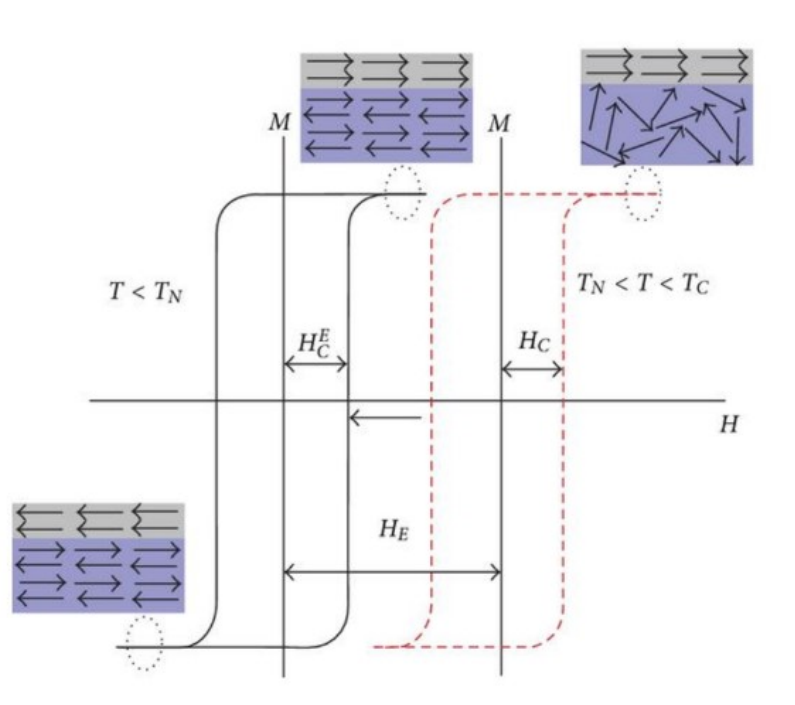


Figure: 1.2 Schematic diagram of FM/AFM bilayer showing exchange bias effect. The grey layer has AFM spin structure, while the violet one represents FM layer. M-H hysteresis loop is shifted along the field axis demonstrating exchange bias at temperature $T < T_N$ [16].

Most commonly studied exchange-biased nanoparticle systems prepared by soft chemical methods are composed of transition metal ferromagnetic cores and the corresponding passivation shell, such as Co/CoO, (Co,Ni)/(Co,-Ni)O, Fe/Fe_xO_y, or Mn/Mn_xO_y, or oxides with different oxidation states, as in CrO₂/Cr₂O₃ or Fe₃O₄/R-Fe₂O₃

and $\text{Fe}_3\text{O}_4/\text{FeO}$. Recently, controlled core-shell nanoparticles such as $\text{SrFe}_{12}\text{O}_{19}/\text{CoO}$, $\text{CoFe}_2\text{O}_4/\text{MnO}$, or FePt/MnO have also been reported [17-25].

Nickel oxide is a very popular material in either the bulk or nanostructured form due to its useful physicochemical properties, which can be modified for different applications. Nickel oxide has a rock salt structure. It has a Néel temperature of 523 K when measured in bulk material [26]. The Néel temperature is a temperature under which an antiferromagnetic material behaves as an ordered AFM phase and above which it becomes paramagnetic; a similar transition point is referred to as the Curie temperature in case of ferromagnetic materials.

The principal motivation of this thesis study lies in earlier findings from studies made in our lab. Note that core-shell nanostructured systems are commonly either the core-phase/shell-phase or the core-phase@shell-phase convention: Henceforth, I will use the latter convention. In previous studies, a number of $\text{Cr}_2\text{O}_3@\text{M}_x\text{Cr}_{2-x}\text{O}_{3-\delta}$ CSN systems were synthesized exhibiting enhanced magnetic properties that hold promise for potential magnetic applications [27-29]. However, the exchange bias effect in these CSNs has been observed to be considerably reduced at room temperature due to the Néel temperature of the AFM core occurring just above the RT value ($T_N = 308$ K). Bulk NiO generally has AFM ordering with a Néel temperature (523 K) considerably above room temperature, which makes it well suited for bimagnetic core-shell nanostructure applications. Interestingly, with the exception of a very small number of other unimagnetic NiO-based systems, the Ni@NiO CSNs appear to be the only bimagnetic NiO-based CSN system investigated to date [30-35]. Ni@NiO CSNs are typically synthesized by oxidation of Ni nanoparticles, thus producing a NiO shell over the Ni core. These CSNs exhibit high

coercivities at room temperature and, for ones coated with graphitic carbon, superparamagnetic blocking temperatures above room temperature. These effects were attributed to strong exchange bias effects occurring at the interface between the FM core and the AFM shell of the Ni@NiO CSNs.

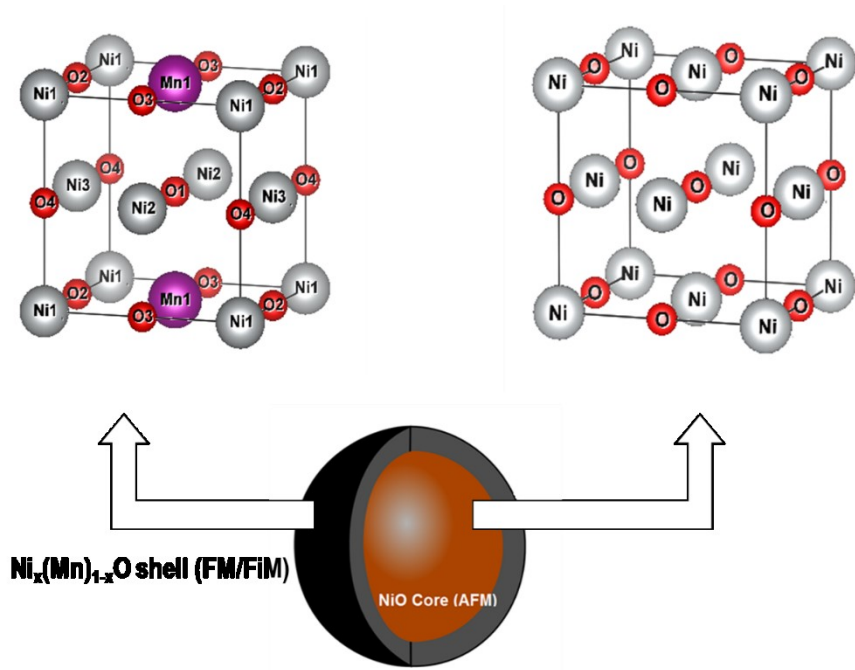


Figure: 1.3 Schematic diagram of synthesized CSNs [36].

The predominant hypothesis of this study is that by using the hydrothermal nanophase epitaxy synthesis technique developed in Mayanovic's lab first using Cr₂O₃-based nanoparticle systems, NiO@Ni_xM_{1-x}O CSNs (M: Mn, Co) having the AFM@FM/FiM magnetic structure could be produced for the first time with potentially novel magnetic properties. The study is divided into two parts. In the first part, the effect of manganese addition and synthesis of NiO@Ni_xMn_{1-x}O (or, Mn-NiO) CSNs was investigated. Different batches of Mn-NiO CSNs were synthesized, having varying Mn x

concentration, using a two-step procedure. The particle size was obtained from two different sources. First, the particle size was obtained using the Scherrer formula applied to the analysis of x-ray diffraction (XRD) data. Then to verify the result, size distribution plots were obtained using transmission electron microscopy (TEM) images. For further detailed structural analysis, a combination of high-resolution TEM (HRTEM), electron dispersive spectroscopy (EDS), and XRD analyses were utilized. Superconducting quantum interface device (SQUID) magnetometry was utilized to obtain hysteresis (magnetization, M Vs field, H) data both at field cooled (FC) and zero field cooled (ZFC) conditions. To complement the experimental results, density functional theory (DFT) based calculations on $Ni_xMn_{1-x}O$ structures were carried out.

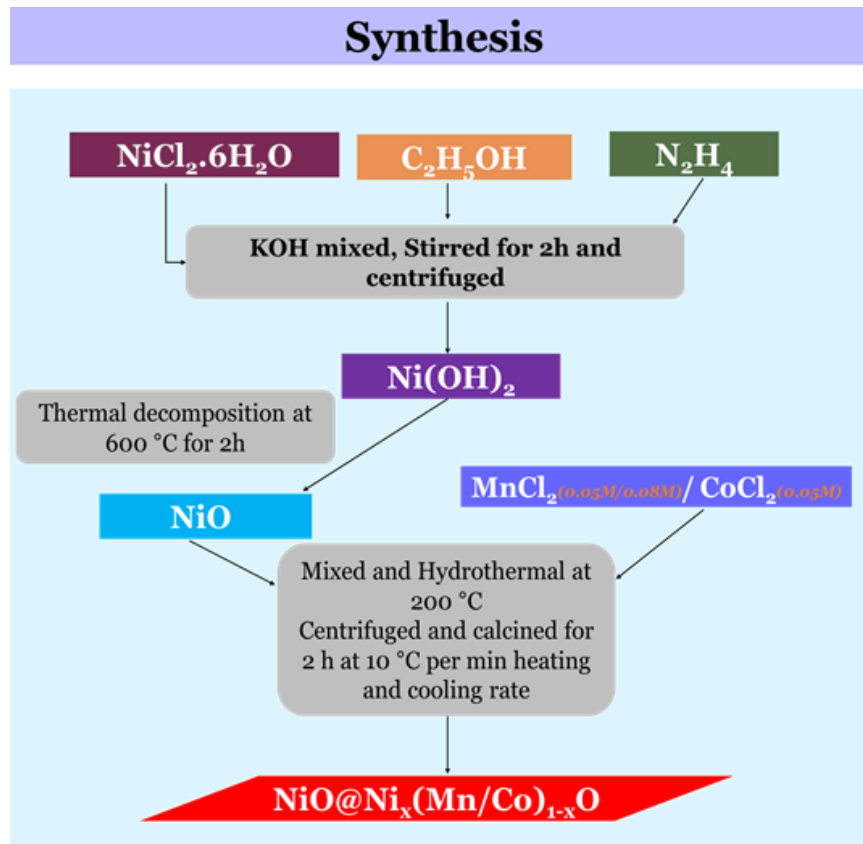


Figure: 1.4 Summary of synthesis procedure [36].

In the second part, the study on cobalt ion incorporation in NiO and synthesis of NiO@Ni_xCo_{1-x}O (or, Co-NiO) CSNs was investigated. The same types of characterization as on the Mn-NiO CSNs were carried out on the Co-NiO CSNs, in order to ascertain their structural and magnetic properties.

CHAPTER 2: SYNTHESIS AND CHARACTERIZATION OF NOVEL INVERTED NiO@Ni_xMn_{1-x}O CORE-SHELL NANOPARTICLES

Abstract

Magnetic core-shell nanoparticles have the potential for numerous applications, such as in magnetic recording media, magnetic resonance imaging, drug delivery or hyperthermia, and spin valves. Inverse core-shell nanoparticles, comprised of an antiferromagnetic (AFM) core covered by a ferromagnetic (FM) or ferrimagnetic (FiM) shell, are of current interest due to the tunability of their magnetic properties. NiO is typically antiferromagnetic in nature and has a Néel temperature of 523 K. Our primary objective in this project is to synthesize and characterize inverted core-shell nanoparticles (CSNs) comprised of a NiO (AFM) core and a shell consisting of a Ni_xMn_{1-x}O (FM/FiM) compound. The synthesis of the CSNs was made using a two-step process. The NiO nanoparticles were synthesized using a chemical reaction method. Subsequently, the NiO nanoparticles were used to grow the NiO@Ni_xMn_{1-x}O CSNs using our hydrothermal nano-phase epitaxy method. XRD structural characterization shows that the NiO@Ni_xMn_{1-x}O CSNs have the rock salt cubic crystal structure throughout. SEM-EDS data indicates the presence of Mn in the CSNs. SQUID magnetic measurements show that the CSNs exhibit AFM/FM or AFM/FiM characteristics with a coercivity field of 425 Oe at 5 K. The field cooled vs zero field cooled hysteresis loop measurements show a significant exchange bias effect between the AFM NiO core and FM/FiM Ni_xMn_{1-x}O shell of the CSNs. The results of additional TEM and magnetic characterization are discussed.

Introduction

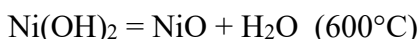
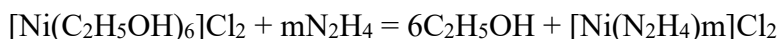
Core-shell nanoparticles (CSNs) have attracted considerable attention due to their potential applications in a number of industrially important areas. The properties of CSNs can be controlled by tuning their core size, shell thickness, composition, surface functionality and other parameters. CSNs have many potential applications in catalysis, materials chemistry, sensors, magnetic random access memory, spintronic devices and biomedical application [1,2]. The physicochemical properties of nanoscale metal oxides depend on particle size, shape, surface area and homogeneity, which in turn depend on the synthesis methods that were used for their preparation. For the synthesis of core-shell nanoparticles, different methods such as homogenous precipitation, co-precipitation, impregnation, sol-gel, sono-chemical, micro-emulsion, hydrothermal, and thermal decomposition methods have been used [3]. The most common research interest area for bi-magnetic core-shell nanoparticles is in controlling the magnetic properties of the core vs the shell. Typically, this is enabled by synthesizing a core having ferromagnetic/ferrimagnetic (FM/FiM) properties whereas the shell has antiferromagnetic (AFM) properties or vice versa. The latter type are referred to as inverted CSNs. Exchange interaction between the AFM core and FM/FiM shell or vice versa results in a shift in field cooled (FC) hysteresis in comparison to zero field cooled (ZFC) hysteresis, which is known as the exchange bias effect. Development of core-shell nanoparticles with a Curie temperature (T_C) above room temperature is highly desirable for device applications such as hypothermia treatment. The most common form of CSNs have transition metal cores and its oxide as a shell. (e.g. Ni@NiO) [4]. In our research work, we use transition metal NiO as the core, which is generally antiferromagnetic in nature.

Pure nickel oxide in the bulk form undergoes antiferromagnetic ordering at a Néel temperature $T_N = 523\text{K}$, which is well above room temperature. The magnetic properties of Mn-doped NiO have been theoretically calculated by Swaststinag et al. using Density Functional Theory (DFT) based calculations [6]. The authors have predicted ferromagnetic properties in Mn-doped NiO. The net magnetization increases with increasing Mn concentration and achieves a maximum at 9.375 at% in their DFT calculations. Considering the AFM nature of NiO and the FM nature of Mn doped NiO, herein I report our investigation on the structural and magnetic properties of inverted $\text{NiO}@\text{Ni}_x\text{Mn}_{1-x}\text{O}$ CSNs prepared using our hydrothermal nanophase epitaxy method [6,7]. The CSNs have been characterized using scanning electron microscopy (SEM), x-ray diffraction (XRD), transmission electron microscopy (TEM), temperature dependent magnetization (M vs T) and (M vs H) hysteresis measurements.

Experimental

NiO nanoparticles were synthesized using the process that was described by El-Kemary et. al [8]. The nanoparticles were synthesized using thermal decomposition of $\text{Ni}(\text{OH})_2$. Nickel chloride hexahydrate (0.111 M) dissolved in absolute ethanol was used as a precursor and was added to hydrazine monohydrate solution (6.73 ml of molar ratio 5). The pH was adjusted from 8.0 to 12 using KOH. The reaction was stirred for ~2 hours at room temperature. Thereafter, the resultant product was washed thoroughly with deionized water for removal of reaction residues and subsequently centrifuged. Finally, nanoparticles [$\text{Ni}(\text{OH})_2 \cdot 0.5\text{H}_2\text{O}$] were formed, and dried. The nickel hydroxide nanoparticles were converted to NiO via thermal decomposition at $600\text{ }^\circ\text{C}$ for ~2 hours.

During the synthesis of NiO nanoparticles, it is reasonable to propose the following reactions:



A quantity of 0.33g NiO nanoparticles was used to synthesize the NiO@Ni_xMn_{1-x}O CSNs using a hydrothermal method at 200 °C for 16 hours. First, distilled water was purged with N₂ for 15 minutes at 70 °C. Next, 0.1265 g (0.05M) MnCl₂ was poured and sonicated for 10 minutes. The pH of the solution was 5.3. Subsequently, NiO nanoparticles were added to the solution and sonicated for 30 minutes. After proper mixing, the solution was inserted inside an autoclave and hydrothermal treated. The resulting CSNs were rinsed, centrifuged and subsequently dried.

SEM structural and morphological study was made using an FESEM (FEI-Quanta 200) instrument operating at 20 kV. The SEM imaging was made by mounting the samples on carbon tape. Preliminary elemental analysis was made with the use of SEM-EDS and a field emission gun (Oxford Instruments). XRD measurements were made using a Bruker D8 Discover instrument operating at 40 kV and 40 mA. The XRD instrument uses a characteristic X-ray source Cu tube (Cu K α , $\lambda = 1.54184 \text{ \AA}$). A Göbel mirror and a 0.6 mm slit were used in the incident side of the x-ray beam and a Linxeye 1-D Si strip detector was used to measure the signal. Structural parameters were extracted

from the XRD patterns using the Bruker TOPAS full-pattern refinement program. The background function for the XRD pattern was modelled using a Chebychev polynomial of 5-th order.

The magnetic measurements were made using a SQUID MPMS/XL magnetometer (Quantum Design, USA). The CSNs were packed in a gelatin capsule without any filler, which was then inserted inside the SQUID magnetometer. Magnetization vs temperature data were measured at temperatures varying between 5 – 330 K. In case of field-cooled (FC) magnetization vs temperature measurements, the applied field was set at 500 Oe. Magnetic hysteresis curve measurements, which were made at 5 K, were made in a range from -5000 to 5000 Oe. For FC hysteresis, the sample was cooled at 5000 Oe. Transmission electron microscopy (TEM) samples were prepared by dispersing the NPs in acetone and depositing samples on lacey carbon grids. TEM analysis was performed using a Titan 80-300 with the field emission gun operated at 300 keV.

Results and Discussion

Figure 2.1 (a) shows an SEM image of synthesized CSNs. It is evident that the CSNs are pseudo spherical in shape. A Gaussian fit of the histogram plot of particle size distribution based on Low resolution TEM image, which is shown in Figure 2.2(b), gives an average particle size of 24.1(3) nm for the $\text{NiO}@_{\text{Ni}_x\text{Mn}_{1-x}}\text{O}$ CSNs. Figure 2.3 shows a high resolution TEM (HRTEM) image of an isolated CSN. It is evident from the image that the core and shell are separated by an interface, which is slightly more structurally disordered than either the core or the shell of the CSN. The TEM image shown in Figure 2.2(a) indicates presence of faceted as well as pseudo spherically shaped CSNs. The shell

region of the nanoparticle shown in Figure 2.1 is not completely uniform as the core NiO nanoparticle is pseudo spherical in shape. The approximate thickness of the shell, estimated from TEM, is ~ 1.3 nm (using imageJ). It is evident from the SEM EDS results shown in Figure 2.1(b) that Mn is incorporated in our CSNs. Prior to CSN synthesis; SEM-EDS results show 50 at% Ni and 50 at% O for the NiO nanoparticles. After CSN formation, it is clear from our SEM-EDS results that 1.59 at% Mn substitution for Ni was accomplished in the shell of the CSNs. The TEM-EDS elemental analysis also confirms the presence of Mn in the CSNs. The shell and core regions of the CSNs, respectively, have identical crystallographic symmetry, as evidenced from our TEM and XRD results (see below), providing evidence of epitaxial growth of the shell.

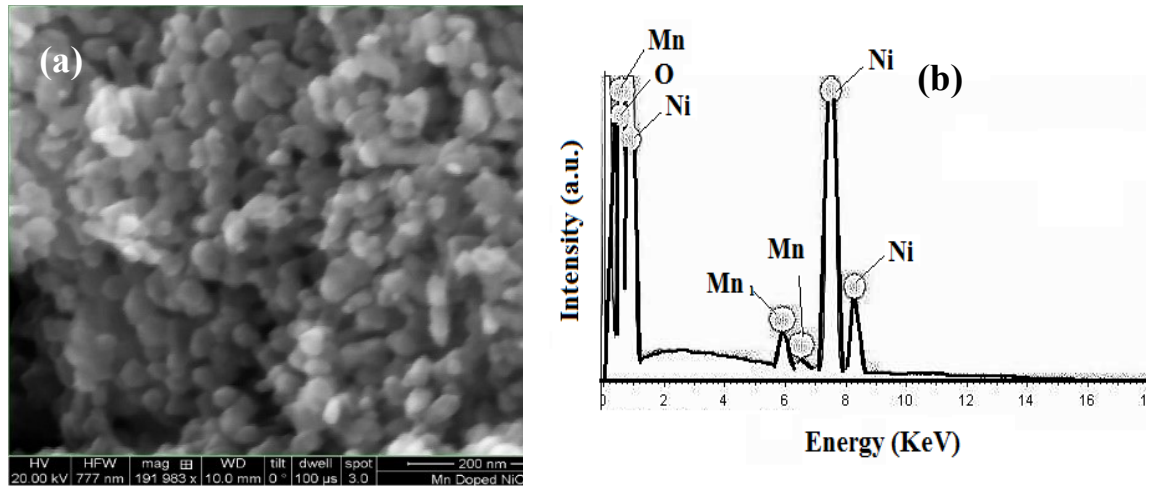


Figure 2.1: (a) SEM image of NiO@Ni_xMn_{1-x}O and (b) corresponding EDX spectra

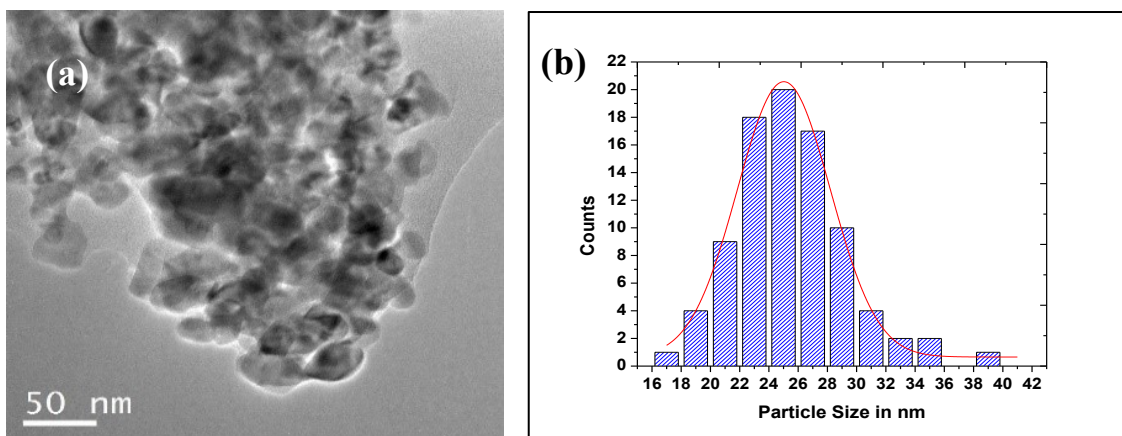


Figure 2.2: (a) Low resolution TEM image of $\text{NiO}@\text{Ni}_x\text{Mn}_{1-x}\text{O}$ and (b) size distribution of particles

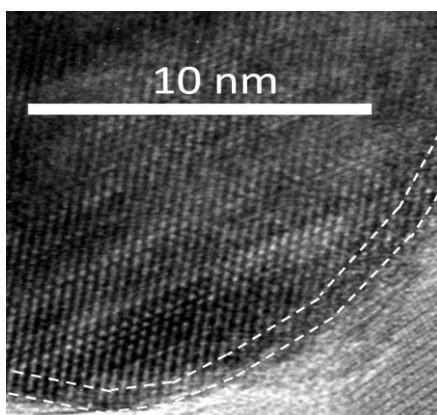


Figure 2.3: High-resolution TEM image of $\text{NiO}@\text{Ni}_x\text{Mn}_{1-x}\text{O}$

Figure 2.4 shows the powder x-ray diffraction pattern measured from our CSNs at room temperature. XRD analysis indicates that the CSNs possess the FCC structure with space group $Fm\bar{3}m$. The values for the ionic radii of Ni^{2+} , Mn^{2+} , Mn^{3+} and Mn^{4+} are 0.69, 0.67, 0.58 and 0.53 Å, respectively [9]. As the difference between ionic radii between Ni^{2+} and Mn^{2+} is small, divalent Mn can replace Ni^{2+} ions without changing the crystal structure. No evidence of impurity phases (e.g., Ni in metallic form, Mn_2O_3 , MnO_2 , or spinel phase NiMn_2O_4) was found in the XRD data. It is evident after the comparison of the XRD patterns measured from our NiO nanoparticles and

NiO@Ni_xMn_{1-x}O CSNs that both have the Fm $\bar{3}$ m symmetry. The average crystallite sizes calculated from the XRD peak broadening, after correction from the instrumental broadening, using the Scherrer formula for NiO is 20.64(3) nm. The size of our NiO@Ni_xMn_{1-x}O CSNs calculated using the Scherrer formula was found to be 23.97(2) nm. This is in very good agreement with the average value of our particle size distribution calculated from the SEM imaging. Clearly, the increase in nanoparticle size indicates Mn incorporation in the shell region, which, based on the XRD analysis has an average thickness of about 1.7 nm. The higher intensity of the (220) peak (located at 62.13°) compared to the usual ratio of peak intensities for bulk NiO suggests oriented nanocrystalline structures. Rietveld refinement of the XRD data measured from the CSN sample was made in order to further analyze their structural properties. The space group of the Fm $\bar{3}$ m FCC structure, with Ni atoms at $x = \frac{1}{2}$, $y = \frac{1}{2}$, and $z = \frac{1}{2}$ and oxygen atoms at $x = 0$, $y = 0$ and $z = 0$ unit cell positions used as starting parameters, was used to account for the core of the CSNs during the refinement of the XRD data. A second Fm $\bar{3}$ m CIF file, based on the Ni_xMn_{1-x}O composition, was added to account for the shell region in the refinement. Our analysis shows that fitting is improved by the addition of the shell in the Rietveld refinement analysis: the Rwp value was reduced by use of a core-shell structure model in comparison to using a single structure model. The lattice parameters and the unit cell volume were found to be increased slightly due to Mn doping in the shell region. Therefore, Mn-incorporation results in a modification of the structure of the shell region of the CSNs, which can affect the magnetic properties indirectly due to changes in the sub-lattice magnetization [8].

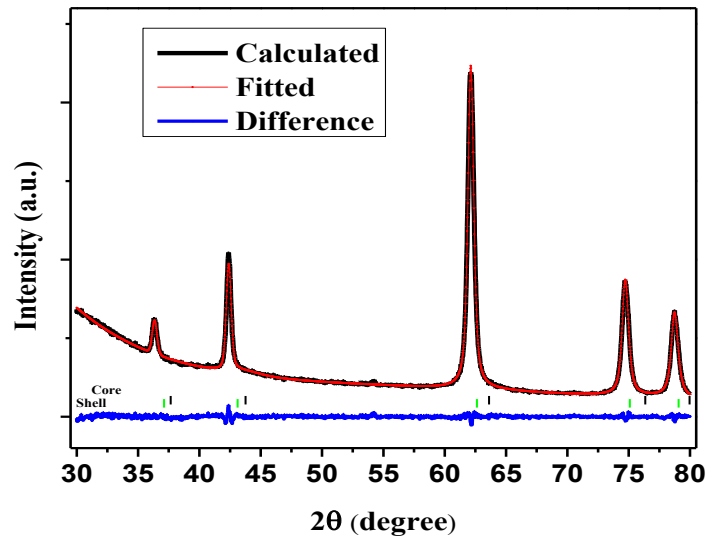


Figure 2.4: Rietveld refinement profile of the powder XRD pattern of CSNs

The magnetization (M) as a function of applied field (hysteresis loop) measured at 5 K is shown in Figure 2.5(a). My preliminary measurements clearly show that the magnetization of the CSNs increases linearly with increasing field and does not reach a saturation value even up to the highest applied field of 5000 Oe. The hysteresis shows a coercive field of about 425 Oe for the zero-field cooled (ZFC) and 500 Oe for the FC case at 5 K. NiO is typically antiferromagnetic in nature. Ferromagnetism has been reported previously in Mn doped NiO nanoparticles by Layek et. al [10]. The hysteresis loops show a significant shift either in the negative (FC) or positive (ZFC) H axis direction and positive (FC) and negative (ZFC) M axis direction, respectively, indicating a substantial exchange bias between the core and shell regions of the CSNs. The value of the exchange bias is ~ 130 Oe between FC and ZFC curves based on the formula $H_e = (H_{ZFC+} - H_{FC+} - H_{FC-} + H_{ZFC-})/2$ where the +/- indicate positive/negative H values when

$M=0$ [11]. It is clear that introduction of Mn^{2+} ions for Ni^{2+} ions in the NiO structure results

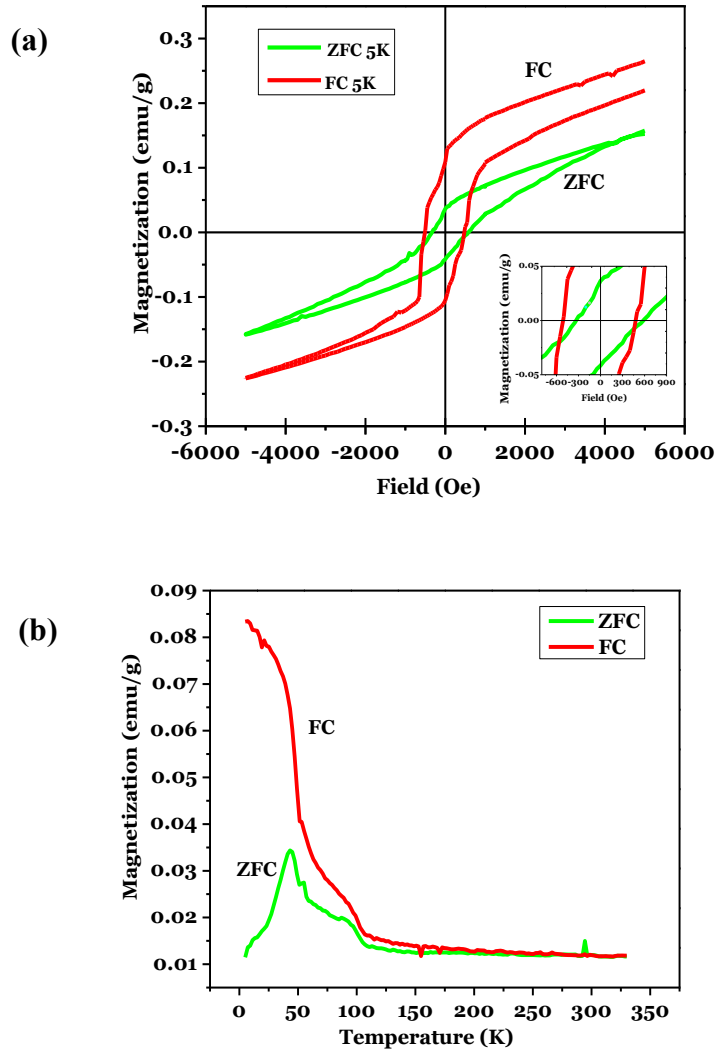


Figure 2.5: (a) Zero field cooled (ZFC) and field cooled (FC) magnetization vs applied field (M vs H) measurement data for $NiO@Ni_xMn_{1-x}O$ CSNs (at 5 K temperature) for 0.05 M Mn precursor concentration: The inset shows the data near the $H = 0$ Oe region (b) Magnetization vs temperature data (range 5 K to 330 K)

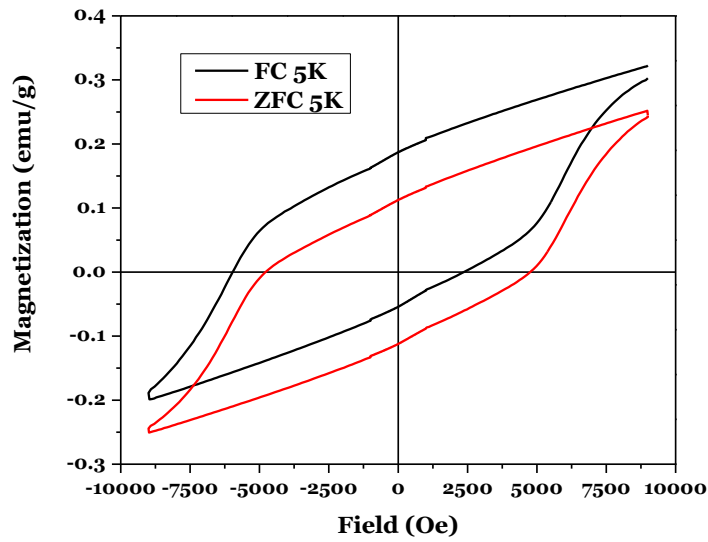
in FM/FiM properties of the shell region. The magnetization data suggests that the core of the CSNs is AFM. Figure 2.5(b) shows the ZFC and FC magnetization, in the 5 to 330 K temperature range, measured from the CSNs. The FC magnetization increases slowly

from 330 K down to ~105 K, more rapidly to ~45 K, and even more abruptly with lower temperature. Conversely, the ZFC magnetization increases slowly up to ~90 K, exhibits a shoulder near 105 K, and then peaks at ~45 K. I speculate that the peak at ~45 K is due to a spin order/disorder transition.

I synthesized an additional batch of CSNs using 0.08M concentration precursor MnCl_2 . The magnetic results of these CSNs were found to be most interesting. The magnetization (M) as a function of applied field (hysteresis loop) measured at 5 K is shown in Figure 2.6 (a). The hysteresis data show a coercive field of ~4787 Oe for the zero-field cooled (ZFC) condition at 5 K. The hysteresis loops show a significant shift in the negative (FC) field axis direction and positive (FC) M axis direction. The value of the exchange bias is ~1729 Oe between FC and ZFC curves. Figure 2.6 (b) shows the ZFC and FC magnetization, in the 5 to 330 K temperature range, measured from our CSNs. The FC magnetization increases slowly from 330 K down to ~70 K, more rapidly to ~40 K, and even more abruptly with lower temperature. The ZFC magnetization increases slowly up to ~70 K and then peaks at ~40 K. The FC magnetization similarly increases slowly up to ~70 K and then rapidly to ~40 K where it begins to level off.

Figure 2.7 shows the change in coercivity with respect to temperature. The data were fitted using an exponential decay function in Origin. The exchange bias field also shows a similar exponential decay dependence as a function of temperature. The details of the fitting of the exchange bias data are shown in the Appendix.

(a)



(b)

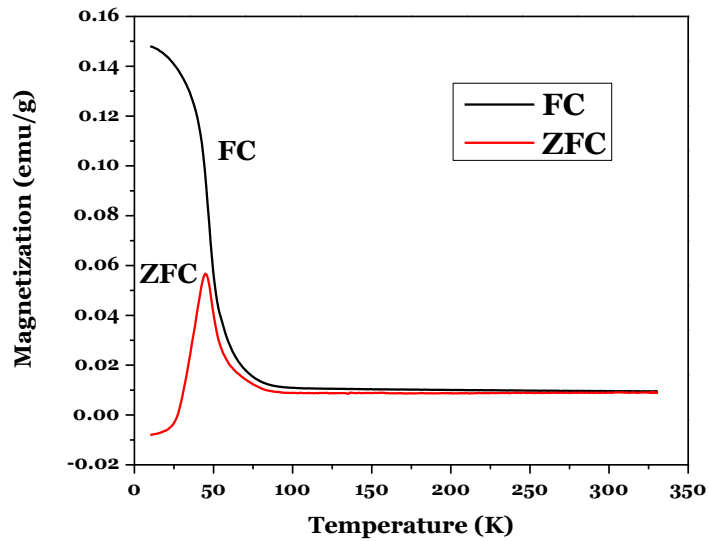


Figure 2.6: (a) Zero field cooled (ZFC) and field cooled (FC) magnetization vs applied field (M vs H) measurement data for NiO@Ni_xMn_{1-x}O CSNs (at 5 K temperature) with 0.08M precursor concentration (b) Magnetization vs temperature data (range 5 K to 330 K)

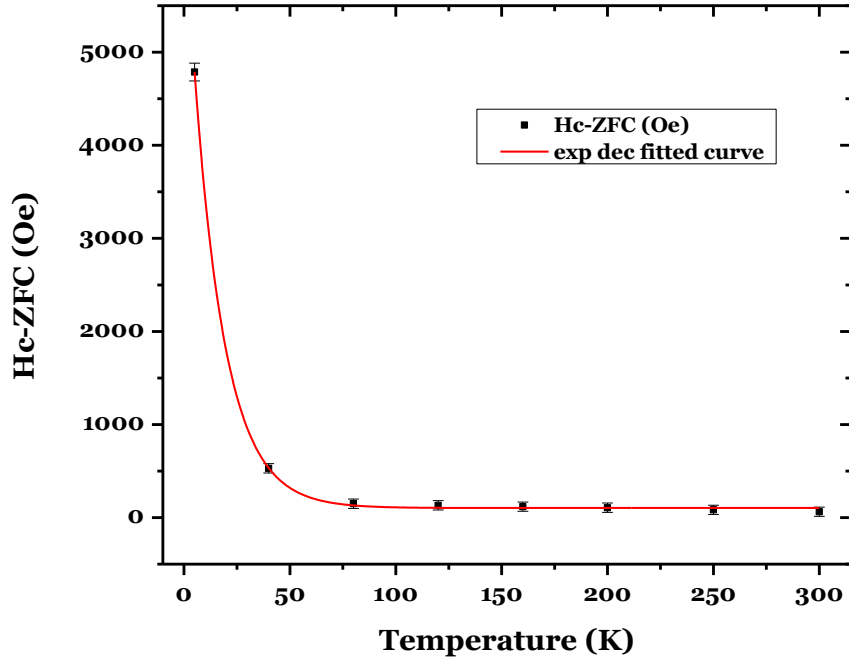


Figure 2.7: Coercivity vs Temperature for 0.08M precursor used CSNs.

The first principles calculations were made using the local spin density approximation method (LSDA) implemented in Quantum Espresso. A rhombohedral primitive unit cell of NiO with a space group of $Fm\bar{3}m$ (COD 4329325) was used for the self-consistent field calculations. The $Ni_{0.88}Mn_{0.12}O$ structure was constructed by replacement of one of the Ni (out of 8 cation sites) with Mn in the 1 x 2 x 2 supercell (Figure 2.8). Calculation convergence was achieved with a net antiferromagnetic configuration (+-+) for the NiO structure. The Brillouin zone integral 6 x 6 x 6 point grid was used based on the Monkhorst–Pack scheme. In order to describe the electron-electron correlation characteristics of local electrons in transition metal atoms, we have performed the GGA+U type calculation where U is the on-site Coulomb energy, U and the exchange interaction (J) were used.

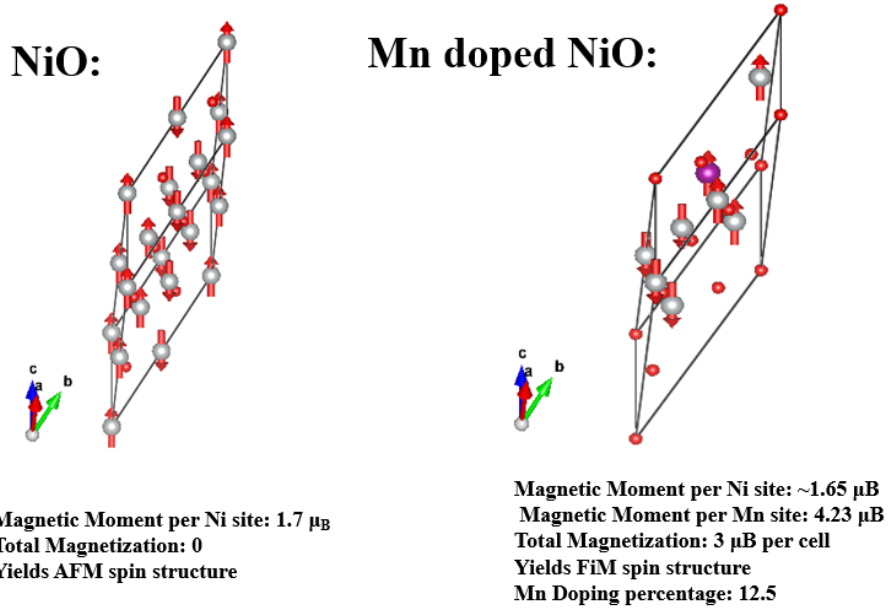


Figure 2.8. Spin Orientation of supercell

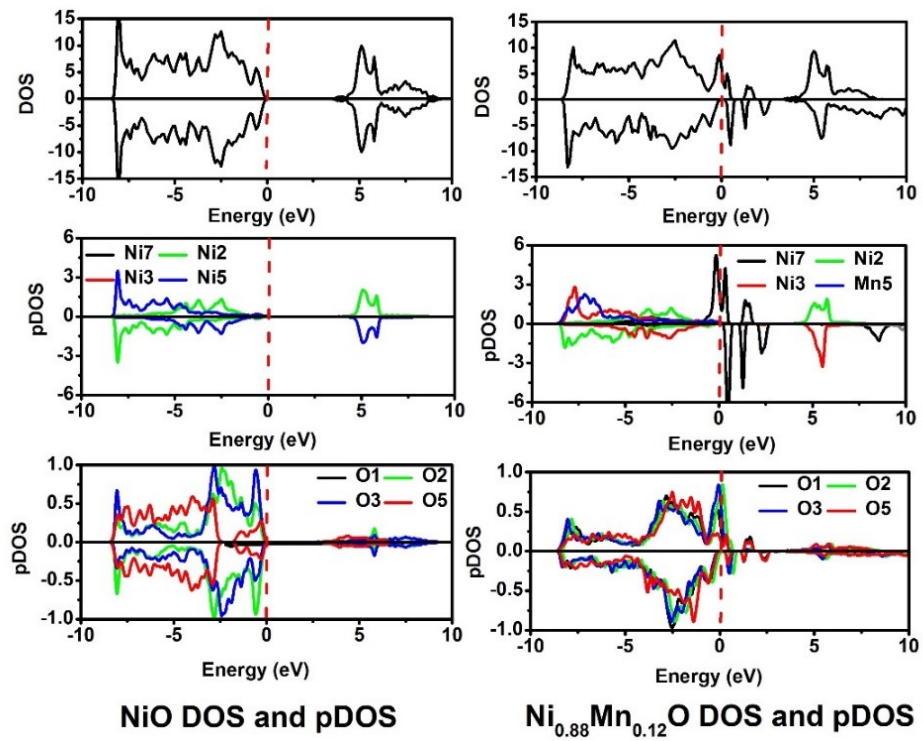


Figure 2.9. DOS and partial DOS (pDOS) from our DFT-based calculations of NiO (left panels) and Ni_{0.88}Mn_{0.12}O (right panels)

Table 2.1. Magnetic moment of individual atom in NiO and structure Ni_{0.88}Mn_{0.12}O

Atom	Magnetic moment (NiO) (μB)	Magnetic moment (Ni _{0.88} Mn _{0.12} O) (μB)
Ni1	1.7	1.688
Ni2	-1.7	-1.6873
Ni3	1.7	1.6896
Ni4	-1.7	-1.6889
Ni5/Mn5	1.7	4.3842
Ni6	-1.7	-1.6972
Ni7	1.7	1.7321
Ni8	-1.7	-1.698

Figure 2.9 shows the calculated density of states (DOS) and the partial DOS (pDOS) of the Ni 3d and O 2p orbitals of NiO and the Ni (Mn) 3d and O 2p orbitals of Ni_{0.88}Mn_{0.12}O, respectively. The value of the calculated energy band gap of NiO is 3.6 eV (as determined by the separation between the O 2p and Ni t_{2g} orbitals): The Fermi level is positioned at the top of the valence band (VB) in the DOS. The calculated magnetic moment of each of the Ni atoms in NiO was found to be 1.7 μB . My calculations show that the introduction of Mn in the NiO structure results in the formation of impurity energy levels (IELs) midway in the band gap of Ni_{0.88}Mn_{0.12}O. The DFT calculations show a considerable shortening of the band gap (~ 2.5 eV) in Ni_{0.88}Mn_{0.12}O. Table 2.1 shows the results of the individual Ni or Ni/Mn atomic magnetic moments in the NiO and Ni_{0.88}Mn_{0.12}O structures, respectively. There is a small redistribution of the magnetic moments among the Ni's in Ni_{0.88}Mn_{0.12}O: Due to the significant difference in the Mn vs

Ni moments and AFM coupling, the resultant spin-ordered configuration is FiM. The overall magnetic moment is $\sim 2.7 \mu\text{B}/\text{cell}$ in $\text{Ni}_{0.88}\text{Mn}_{0.12}\text{O}$. The strong FiM result for $\text{Ni}_{0.88}\text{Mn}_{0.12}\text{O}$ from our DFT based calculations is consistent with our magnetic measurements made of our CSNs.

Conclusions

We used a two-step process, involving thermal decomposition and hydrothermal synthesis, to make $\text{NiO}@\text{Ni}_x\text{Mn}_{1-x}\text{O}$ CSNs. Our characterization confirms Mn ion incorporation in the shell region of the CSNs. XRD analysis shows that both core and shell regions have the FCC structure. TEM analysis confirms the core-shell structure and epitaxial growth of the shell region over the core region of the $\text{NiO}@\text{Ni}_x\text{Mn}_{1-x}\text{O}$ CSNs. SQUID magnetometry results are consistent with an AFM core and an FM/FiM shell, which results in a substantial exchange bias in the CSNs at 5 K. My DFT based calculation also supplements experimental data.

References

1. N. Bayal and P. Jeevanandam, *J. Alloys Compd.* 537, 232 (2012).
2. N.J. Borys, M.J. Walter, J. Huang, D.V. Talapin, and J.M. Lupton, *Science* 330, 1371–1374 (2010).
3. M.B. Gawande, A. Goswami, T. Asefa, H. Guo, A.V. Biradar, D.-L. Peng, R. Zboril, R.S. Varma, *Chem. Soc. Rev.* 44, 7540–7590 (2015).
4. N. Rinaldi-Montes, P. Gorria, D. Martínez-Blanco, A.B. Fuertes, L.F. Barquín, J.R. Fernández, I. de Pedro, M.L. Fdez-Gubieda, J. Alonso, L. Olivi, G. Aquilanti, I. Puente-Orench, and J.A. Blanco, *J. Phys. Conf. Ser.* 663, 12001 (2015).

5. E. Swatsitang and A. Pimsawat, *Adv. Mater. Res.* 55–57, 857 (2008).
6. M.D. Hossain, S. Dey, R.A. Mayanovic, and M. Benamara, *MRS Adv.* 1, 2387 (2016).
7. S. Dey, M.D. Hossain, R.A. Mayanovic, R. Wirth, R. A. Gordon, *J. Mater. Sci.* 52, 2066 (2017).
8. M. El-Kemary, N. Nagy, and I. El-Mehasseb, *Mater. Sci. Semicond. Process.* (2013).
9. R.D. Shannon, *Acta Crystallogr. Sect. A* 32, 751 (1976)
10. S. Layek and H.C. Verma, *J. Magn. Magn. Mater.* 397, 73 (2016).
11. H. Khurshid, S. Chandra, W. Li, M.H. Phan, G.C. Hadjipanayis, P. Mukherjee, and H. Srikanth, *J. Appl. Phys.* **113**, 17B508 (2013).

CHAPTER 3: INVESTIGATION OF NOVEL INVERTED NiO@Ni_xCo_{1-x}O CORE-SHELL NANOPARTICLES

Abstract

Inverse core-shell nanoparticles, comprised of an antiferromagnetic (AFM) core covered by a ferromagnetic (FM) or ferrimagnetic (FiM) shell, are of current interest due to their different potential application and due to the tunability of their magnetic properties. The antiferromagnetic nature of NiO and high Néel temperature (523 K) makes this material well suited for inverse core-shell nanoparticle applications. Our primary objective in this project has been to synthesize and characterize inverted core-shell nanoparticles (CSNs) comprised of a NiO (AFM) core and a shell consisting of a Ni_xCo_{1-x}O (FiM) compound. The synthesis of the CSNs was made using a two-step process. The NiO nanoparticles were synthesized using a chemical reaction method. Subsequently, the NiO nanoparticles were used to grow the NiO@Ni_xCo_{1-x}O CSNs using our hydrothermal nano-phase epitaxy method. XRD structural characterization shows that the NiO@Ni_xCo_{1-x}O CSNs have the rock salt cubic crystal structure. SEM-EDS data indicates the presence of Co in the CSNs. Magnetic measurements show that the CSNs exhibit AFM/FiM characteristics with a small coercivity field of 30 Oe at 5 K. The field cooled vs zero field cooled hysteresis loop measurements show a magnetization axis shift which is attributed to the exchange bias effect between the AFM NiO core and an FiM Ni_xCo_{1-x}O shell of the CSNs. Our ab initio based calculations of the Ni_xCo_{1-x}O rock salt structure confirm a weak FiM character and a mott hubbard insulator property of the compound.

Introduction

Bimagnetic core-shell nanoparticles (CSNs) are of considerable interest due to their potential applications in magnetic spin valves, spintronics, magnetic random access memory, hyperthermia, MRI imaging, drug delivery and in other areas [1–4]. The magnetic properties of bimagnetic CSNs (without being embedded in a surrounding matrix) are tuned by adjustment of overall size, core vs shell size, core vs shell composition, and morphology. Core-shell nanoparticles are typically fabricated in a conventional configuration, having a ferromagnetic (FM) core and an antiferromagnetic (AFM) or ferrimagnetic (FiM) shell, or in an inverted configuration, having an AFM core and a FM or FiM shell. Due to their highly ordered AFM cores, the inverted bimagnetic CSNs have highly tunable coercivities, blocking temperatures, and other magnetic properties that are highly promising for device and medicinal applications. There has been particular attention paid to the exchange bias effect in bimagnetic CSNs, whereby a magnetic interaction between the core and shell has a direct bearing on the overall magnetic properties of the nanostructures [5,6]. By suitable tuning of the CSNs in terms of composition, size and morphology characteristics alluded to above, the exchange bias properties can potentially be exploited for various magnetic device and medicinal applications.

In our lab, it has been recently investigated a number of $\text{Cr}_2\text{O}_3@M_x\text{Cr}_{2-x}\text{O}_{3-\delta}$ CSN systems and found these to have enhanced magnetic properties that show promise for potential magnetic applications [7-9]. However, the exchange bias effect in these CSNs has been observed to be considerably reduced at room temperature due to the Néel temperature of the AFM core occurring just above the RT value ($T_N = 308$ K). Bulk NiO

generally has AFM ordering with a Néel temperature considerably above room temperature ($T_N = 523$ K), which makes it well suited for bimagnetic core-shell nanostructure applications. Remarkably, to my knowledge, with the exception of a very small number of other systems, the Ni@NiO CSNs appear to be the overwhelmingly predominant bimagnetic NiO-based core-shell nanostructure system that has been investigated to date [10–15]. The synthesis of Ni@NiO CSNs typically involves synthesis of the Ni nanoparticles followed by their oxidation, thus producing a NiO shell over the Ni core. These CSNs have been shown to exhibit high coercivities at room temperature and, for ones coated with graphitic carbon, superparamagnetic blocking temperatures at above room temperature value. In both cases, these effects were attributed to substantial exchange bias effects occurring at the interface between the FM Ni core and the AFM NiO shell [15]. Recently, Skoropata et al. studied a series of iron oxide based core-shell nanostructures, including Fe_2O_3 @NiO CSNs [16]. Their conclusion was that the magnetic properties of the Fe_2O_3 @NiO CSNs were consistent with the formation of an inter-diffused Ni-doped Fe_2O_3 layer at the core-shell interface, resulting in a trilayer nanostructure. Although most likely not bimagnetic, it has been reported that SiO_2 @NiO CSNs exhibit greater remanent and saturation magnetization values, but lower coercivities, than NiO nanoparticles [17]. Ponnusamy et al. have recently synthesized Co-doped NiO nanoparticles using a chemical reaction method [18]. The authors report that their magnetic measurements reveal ferromagnetic properties in the $\text{Co}_x\text{Ni}_{1-x}\text{O}$ nanoparticles. In this paper, I report on the synthesis and characterization of inverted NiO@ $\text{Ni}_x\text{Co}_{1-x}\text{O}$ CSNs, where the core-shell nanostructure was made using our hydrothermal nanophase epitaxy method.

Experimental

The synthesis of the CSNs was made as follows: NiO nanoparticles were first synthesized according to procedures outlined by El-Kemary et. al [19]. The nanoparticle synthesis was made using thermal decomposition of Ni(OH)₂. A precursor was first prepared using nickel chloride hexahydrate (0.111 M) dissolved in ethanol which was then added to 6.73 ml of hydrazine monohydrate at a solution molar ratio of 5. KOH was used to adjust the pH to about 12 and the solution was stirred for ~2 hours at 22 °C. Upon completion of stirring, the reaction product was rinsed with deionized water for removal of residues and then centrifuged in toluene. The Ni(OH)₂.0.5H₂O nanoparticles were dried in atmosphere. Finally, the nickel hydroxide nanoparticles were converted to NiO nanoparticles through thermal decomposition at 600 °C for ~2 hours.

The NiO nanoparticles were next used as cores to synthesize the NiO@Ni_xCo_{1-x}O CSNs using a hydrothermal method described previously [20]. First, HPLC grade water (pH = 7) was purged with N₂ gas for 15 minutes at 70 °C. Next, 0.237 g CoCl₂.6H₂O were added to the deoxygenated water to make a 0.05 M solution (pH = 5.6) and sonicated for ~30 minutes. Several drops of HCl were added to reduce the pH of the solution to a value of 3.2. Subsequently, 0.33g of NiO nanoparticles was added to the solution, which was then sonicated for ~30 minutes. Subsequently, the solution was inserted inside an autoclave and hydrothermal treated at ~190 °C for 20 hours. The resulting NiO@Ni_xCo_{1-x}O CSNs were then rinsed, centrifuged in DI water and subsequently dried in atmosphere.

The SEM imaging characterization was made using a JEOL SEM instrument operating at 2 kV with WD of 5 mm. The samples were mounted on carbon tape for SEM

imaging. Preliminary elemental analysis was made using a SEM-EDS (Oxford Instruments) and a field emission gun. XRD data were measured from the nanopowder samples using a Bruker D8 Discover diffractometer operating at 40 kV and 40 mA. The diffractometer is operated using a Cu tube x-ray source ($\text{Cu K}\alpha$, $\lambda = 1.54184 \text{ \AA}$), a Göbel mirror and a 0.6 mm slit on the incident x-ray beam. A Linxeye 1-D Si strip detector was used for measurement of the XRD data. The XRD data were analyzed using Rietveld refinement, which was accomplished using the Bruker TOPAS software. The modelling of the background in the XRD patterns was made using a 5-th order Chebychev polynomial.

The magnetization data were measured from the samples using a SQUID MPMS/XL magnetometer (Quantum Design) and a PPMS-VSM instrument at CCMR, Cornell University (Quantum Design). The nanoparticle samples were packed in a gelatin capsule and then inserted inside the dewar of the SQUID magnetometer. The magnetization data were measured in the 5 – 300 K temperature (T) range. An applied field of 500 Oe was used to make the magnetization vs T measurements in the field-cooled (FC) case. The magnetic hysteresis curves were measured at 5 K in the -10,000 to 10,000 Oe applied field range. The samples were cooled at 20,000 Oe in the case of FC hysteresis loop measurements whereas 0 field was applied in the case of zero-field-cooled (ZFC) measurements. The TEM analysis was made using a Titan 80-300 instrument for which the field emission gun was operated at 300 keV. The TEM samples were prepared on lacey carbon grids.

The first principles calculations were made using the local spin density approximation method (LSDA) implemented in Quantum Espresso [21]. A rhombohedral

primitive unit cell of NiO with a space group of $Fm\bar{3}m$ (COD 4329325) was used for the self-consistent field calculations. The $\text{Ni}_{0.88}\text{Co}_{0.12}\text{O}$ structure was constructed by replacement of one of the Ni (out 8 cation sites) with Co in the 1 x 2 x 2 supercell. Calculation convergence was achieved with a net antiferromagnetic configuration (+-+-) for the NiO structure. The Brillouin zone integral 6 x 6 x 6 point grid was used based on the Monkhorst–Pack scheme [22]. The cutoff energy for the plane waves was 150 eV. Structural relaxation (volume) was accomplished for all of the structures and the relaxed structural parameters were used in the final calculation. Density of states (DOS) and the projected density of state (pDOS) were obtained by using the tetrahedron method with an 8 x 8 x 8 k-point grid mesh. Perdew–Burke–Ernzerhof exchange–correlational norm conserving pseudopotentials were used for all the atoms [23]. Additionally, in order to describe the electron–electron correlation characteristics of local electrons in transition metal atoms, we have performed the GGA+U type calculation where U is the on-site Coulomb energy, U and the exchange interaction (J) were used.

Results and Discussions

Figure 3.1 (a) shows an SEM image of synthesized CSNs. A Gaussian fit of the histogram plot of particle size distribution shown in Figure 3.2(b), as determined from TEM imaging, gives an average particle size of 29.7(2) nm for the $\text{NiO}@_{\text{Ni}_x\text{Co}_{1-x}\text{O}}$ CSNs. This is in very good agreement with our XRD Scherrer equation analysis yielding a CSN size of 29.39(6) nm. The SEM-EDS data shown in Figure 3.1 (b) show that Co, along with Ni and O, are present in the sample. Figure 3.3(a, b) shows a high-resolution TEM (HRTEM) image of an isolated CSN. As shown in the TEM image, the core and

shell are separated by an interface which is slightly more structurally disordered than either the core or the shell of the isolated CSN. The SEM and TEM imaging indicate presence of faceted as well as pseudospherically shaped CSNs. The shell region of the nanoparticle shown in Figure 3.3 is not completely uniform as the core NiO nanoparticles are pseudospherical in shape. The approximate thickness of the shell, estimated from the TEM images, is ~ 2 nm. The shell and core regions of the CSNs, respectively, have identical crystallographic symmetry, as evidenced from our TEM and XRD results (Figures 3.3 and 3.4), providing evidence of epitaxial growth of the shell. Figure 3.4

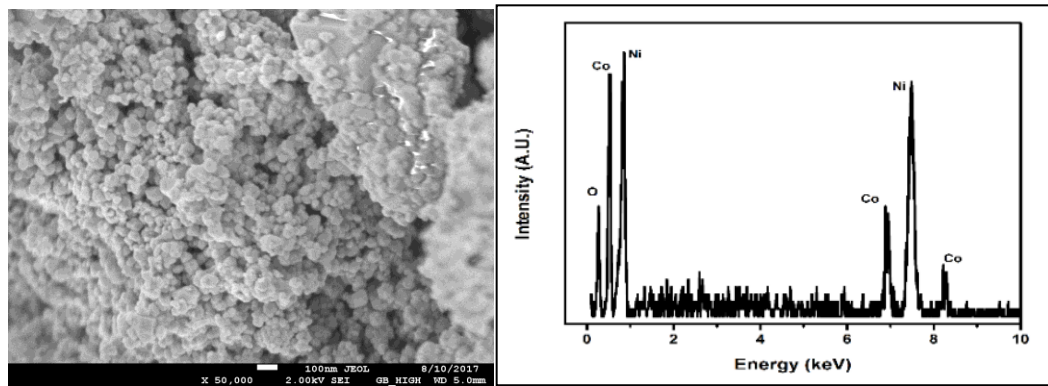


Figure 3.1: (a) SEM image of NiO@Ni_xCo_{1-x}O and (b) corresponding EDX spectra

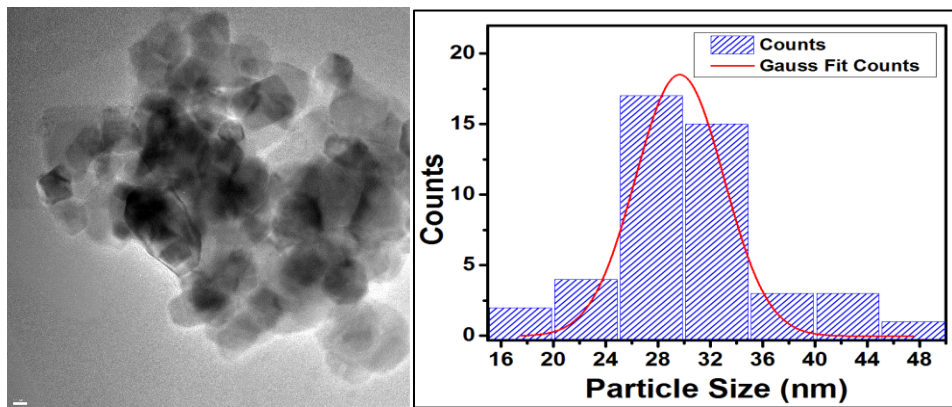


Figure 3.2: (a) Low resolution TEM image of NiO@Ni_xCo_{1-x}O and (b) size distribution of particles;

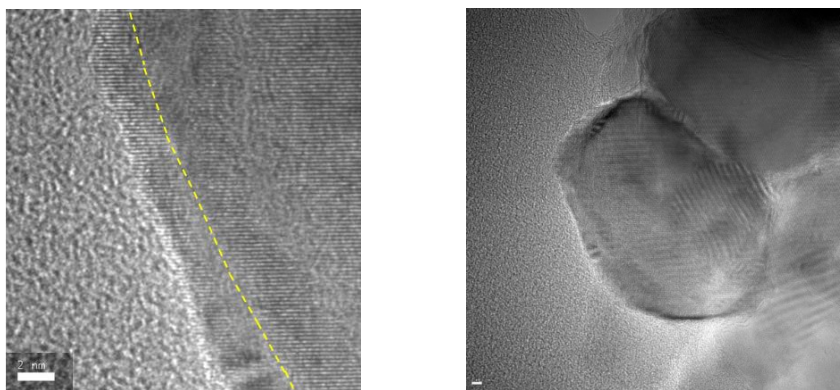


Figure 3.3: High-resolution TEM image of NiO@Ni_xCo_{1-x}O

shows the powder x-ray diffraction pattern measured from our CSNs at room temperature. XRD analysis indicates that the CSNs possess the FCC structure with space group $Fm\bar{3}m$ with a small contribution from a minor cubic phase having the $F\bar{4}3m$ structure: The minor phase is consistent with nanocrystalline Co₃O₄. The values for the ionic radii of Ni²⁺ and Co²⁺ (high spin) are 0.69 and 0.745 Å for six fold coordination, respectively [23,24]. Thus, Co²⁺ can readily substitute for Ni²⁺ ions in the rock salt structure of NiO. The higher intensity of the (200) peak (located at 43.18°) compared to the usual ratio of peak intensities for bulk NiO suggests somewhat oriented nanocrystalline structures. Rietveld refinement of the XRD data measured from the CSN sample was made in order to further analyze their structural properties. Two $Fm\bar{3}m$ structure CIF files were used in the refinement, one for the NiO core and another for the Ni_xCo_{1-x}O shell, and a $F\bar{4}3m$ structure CIF file for the impurity phase. The lattice parameters and the unit cell volume were found to be increased slightly for the Ni_xCo_{1-x}O shell due to Co doping in the shell region, which is consistent with the ionic radii difference between Ni²⁺ and Co²⁺. Therefore, Co-incorporation results in a modification

of the structure of the shell region of the CSNs, which can indirectly affect the magnetic properties of the $\text{Ni}_x\text{Co}_{1-x}\text{O}$ shell. The unusual magnetic behavior may be due to grain size reduction and breaking of large number of exchange bonds. The presence of small magnetic clusters on the surface and lattice imperfection increases the uncompensated spin values [18].

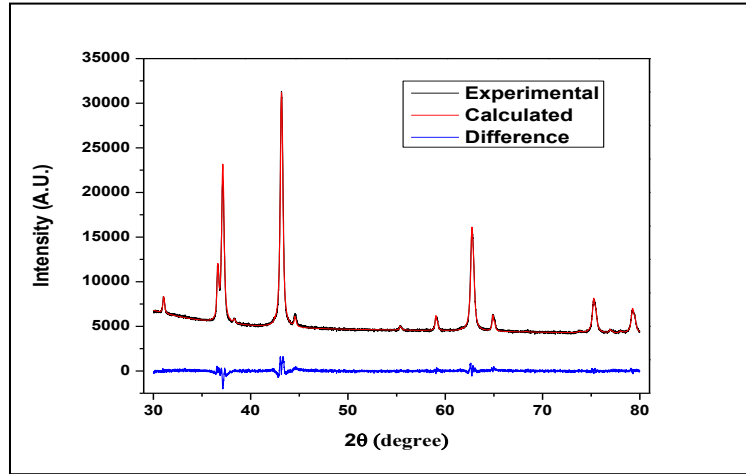
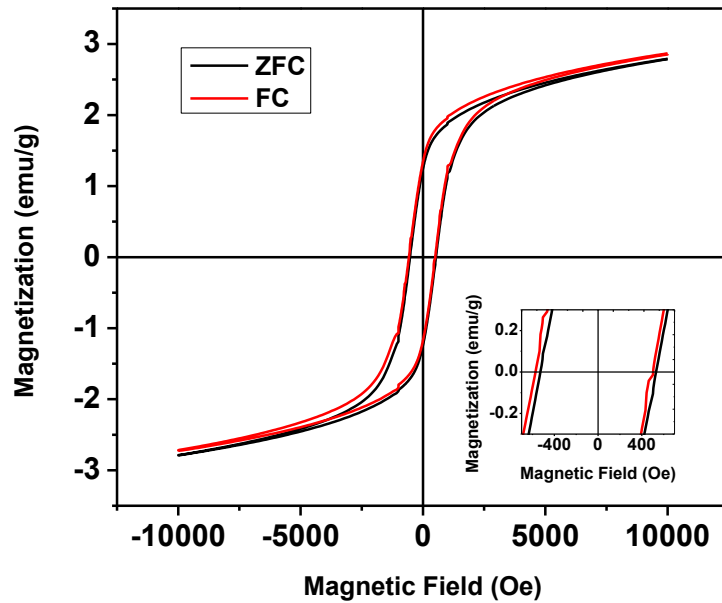
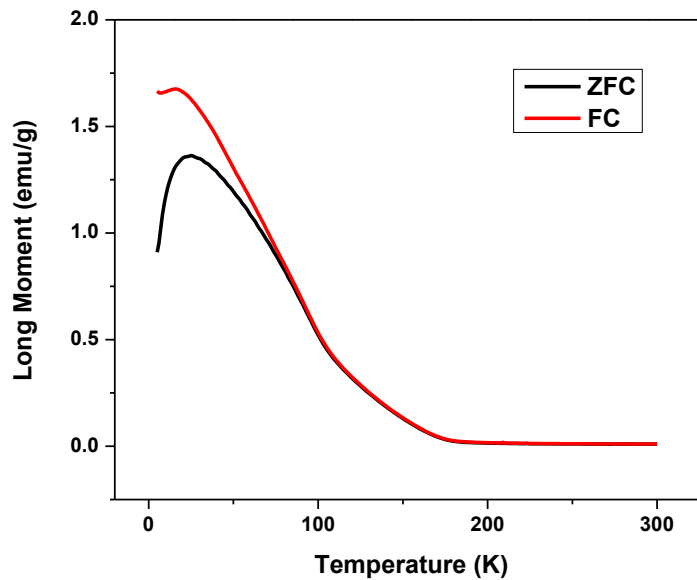


Figure 3.4: Rietveld refinement profile of the powder XRD pattern of CSNs

The magnetization (M) as a function of applied field (hysteresis loop) measured at 5 K is shown in Figure 3.5 (a). Our preliminary measurements clearly show that the magnetization of the CSNs shows a high retentivity value and does not reach a saturation value at 1000 Oe. The hysteresis shows a coercive field of about ~ 528 Oe for the ZFC and ~ 538 Oe for the FC case at 5 K. Ferromagnetism has been reported previously in Co doped NiO nanoparticles by Ponnusamy et. al. [18]. The hysteresis loops show a shift of the FC hysteresis loop relative to the ZFC loop along the negative H axis and positive M axis directions. This is consistent with an exchange bias between the core and shell



a.



b.

Figure 3.5. (a) Zero field cooled (ZFC) and field cooled (FC) magnetization vs applied field (M vs H) measurement data for $\text{NiO}@\text{Ni}_x\text{Co}_{1-x}\text{O}$ CSNs (at 5 K temperature): The inset shows the data near the $H = 0$ Oe region and positive and negative saturation. (b) Magnetization vs temperature data (range 5 K to 300 K) (c) ZFC hysteresis of Co_3O_4 NPs, (d) ZFC hysteresis of NiO NPs

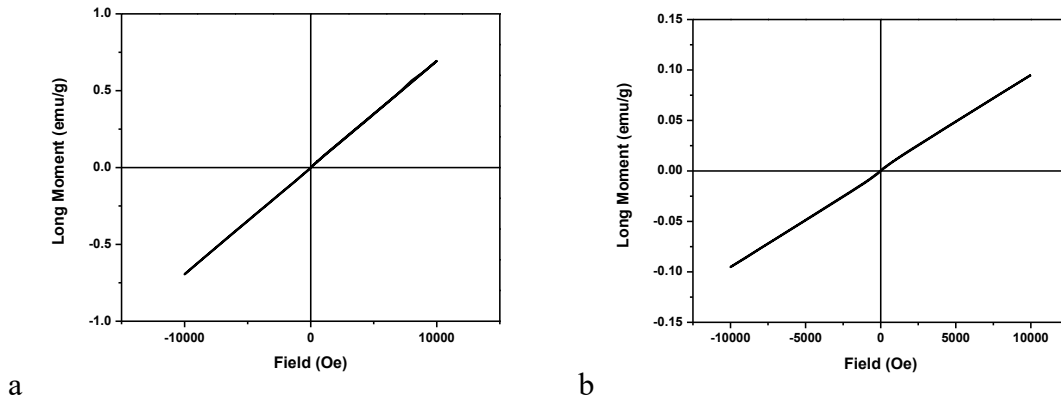


Figure 3.6. (a) ZFC hysteresis of Co_3O_4 NPs, (b) ZFC hysteresis of NiO NPs (both at 5 K)

regions of the CSNs [3]. The value of the exchange bias is ~ 34 Oe between FC and ZFC curves based on the formula $H_e = (H_{ZFC+} - H_{FC+} - H_{FC-} + H_{ZFC-})/2$ where the +/- indicate positive/negative H values when $M = 0$ [25]. It is clear that introduction of Co^{2+} ions for Ni^{2+} ions in the NiO structure results in most likely FiM properties within the shell region of the CSNs. The magnetic data for our NiO and Co_3O_4 NPs indicates that these exhibit AFM properties (Figure 3.6(a) and (b)). Figure 3.5(b) shows the ZFC and FC magnetization vs temperature data measured from our $\text{NiO}@_{\text{Ni}_x\text{Co}_{1-x}\text{O}}$ CSNs. The FC magnetization shows a peak at ~ 20 K followed by a rapid decrease with increasing temperature to ~ 174 K and a very shallow reduction trend thereafter to 300 K. The ZFC magnetization curve increases sharply from 5 K, peaks at ~ 20 K and then declines in a similar manner to 300 K as the FC curve but shows a shoulder near ~ 90 K. The peak at ~ 20 K is potentially a manifestation of a spin order/disorder transition in the CSNs. The shoulder occurring at ~ 90 K may be associated with the superparamagnetic blocking temperature of the CSNs. The bifurcation point between the ZFC and FC magnetization curves is at ~ 100 K.

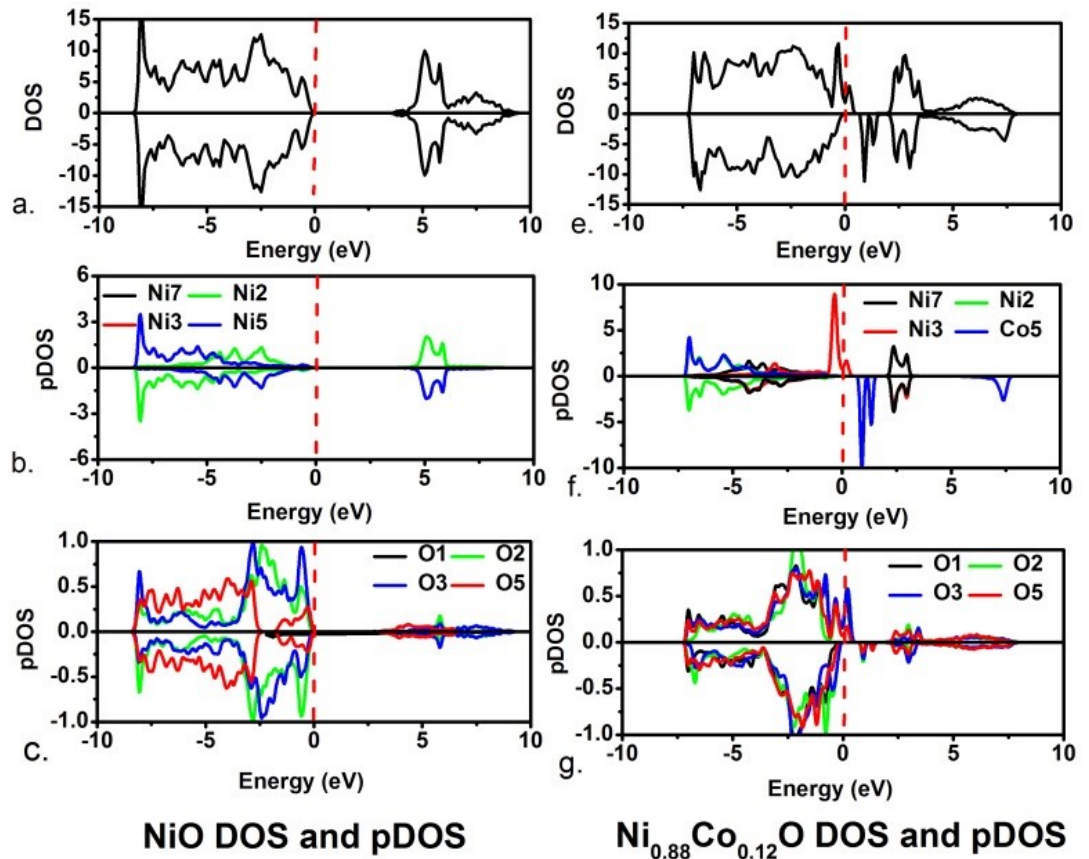


Figure 3.7. DOS and partial DOS (pDOS) from our DFT-based calculations of NiO (left panels) and $\text{Ni}_{0.88}\text{Co}_{0.12}\text{O}$ (right panels)

Figure 3.7 shows the calculated density of states (DOS) and the partial DOS (pDOS) of the Ni 3d and O 2p orbitals of the NiO and the Ni (Co) 3d and O 2p orbitals of the $\text{Ni}_{0.88}\text{Co}_{0.12}\text{O}$ structures, respectively. The calculated energy band gap of NiO is 3.6 eV (defined by the separation between O 2p and Ni t_{2g} orbitals) with the Fermi level positioned at the top of the valence band (VB). Our theoretically calculated band gap value agrees within reason to the experimental value of 3.2–4.0 eV, verifying the validity of our modeling approach. The magnetic moment of each Ni atom was calculated to be 1.7 μB , which is in excellent agreement with experimental results. The Fermi level

Table 3.1. Magnetic moment of individual atom in NiO and structure Ni_{0.88}Co_{0.12}O

Atom	Magnetic moment (NiO) (μB)	Magnetic moment (Ni _{0.88} Co _{0.12} O) (μB)
Ni1	1.7	1.6432
Ni2	-1.7	-1.6768
Ni3	1.7	1.6767
Ni4	-1.7	-1.6382
Ni5/Co5	1.7	1.838
Ni6	-1.7	-1.6806
Ni7	1.7	1.68
Ni8	-1.7	-1.6728

crosses the majority spin energy states in the upper portion of the VB of the DOS of Ni_{0.88}Co_{0.12}O: Because the crossover point occurs in the region where majority Ni 3d p-DOS is dominant near the top of VB and at the bottom of the conduction band (d-d interaction), we conclude that Co_{0.12}Ni_{0.88}O is a Mott-Hubbard insulator. The introduction of Co in the NiO structure results in the formation of impurity energy levels (IELs), which are dominated by Co 3d states, approximately midway in the band gap. In addition, our calculations show an appreciable shortening of band gap (~ 2 eV) in Ni_{0.88}Co_{0.12}O. It should be noted that the incorporation of Co at such a high percentage (12.5%) is above typical doping levels: Thus, there is a considerable effect in the proportion of Co electronic-level contributions in the DOS of Ni_{0.88}Co_{0.12}O, as is evident in the calculated pDOS shown in in the figure. Table 3.1 shows the calculated individual atomic magnetic moments of the cations in the NiO and Ni_{0.88}Co_{0.12}O structures. My

calculations show that the alternate antiparallel spin arrangement, characteristic of AFM structure, is preserved in the equilibrium spin configuration of $\text{Ni}_{0.88}\text{Co}_{0.12}\text{O}$. However, because of the redistribution of the magnetic moments among the Ni's, and the difference in the Co vs Ni moments, the resultant configuration is weak FiM in the ordered spin state. The incorporation of Co results in a magnetic moment of $0.17 \mu\text{B}/\text{cell}$ in $\text{Ni}_{0.88}\text{Co}_{0.12}\text{O}$. The weak FiM result for $\text{Ni}_{0.88}\text{Co}_{0.12}\text{O}$ obtained from calculations is consistent with the magnetic measurements made of the $\text{NiO}@\text{Ni}_x\text{Co}_{1-x}\text{O}$ CSNs.

Conclusions

I have used a two-step process, involving thermal decomposition and hydrothermal synthesis, to fabricate $\text{NiO}@\text{Ni}_x\text{Co}_{1-x}\text{O}$ CSNs. Our characterization confirms Co incorporation in the shell region of the CSNs. XRD and TEM analysis shows that both core and shell regions have the FCC structure. In addition, the TEM analysis confirms the core-shell structure and epitaxial growth of the shell region over the core region of the $\text{NiO}@\text{Ni}_x\text{Co}_{1-x}\text{O}$ CSNs. The magnetometry results are consistent with the presence of an AFM core and an FiM shell in the CSNs exhibiting an exchange bias effect between the two components as observed by a shift along the applied field and magnetization axes. DFT based ab-initio calculations confirm that Co introduction in NiO and formation of $\text{Ni}_x\text{Co}_{1-x}\text{O}$ results in weak FiM properties and in the formation of a Mott-Hubbard insulator.

References

1. J. Wang and X.C. Zeng, in *Nanoscale Magn. Mater. Appl.*, edited by J.P. Liu, E. Fullerton, O. Gutfleisch, and D.J. Sellmyer Springer US, pp. 35–65 (2009)

2. A. Silva, rica Silva-Freitas, J. Carvalho, T. Pontes, R. Arajo-Neto, K. Silva, A. Carrio, and E. Egito, in *Adv. Appl. Biotechnol.*, edited by M. Petre InTech, (2012).
3. A. López-Ortega, M. Estrader, G. Salazar-Alvarez, A.G. Roca, and J. Nogués, *Phys. Rep.* 553, 1 (2015).
4. M.C. Goncalves and M.B. Martins, in *Nanomed. One Central Press*, Manchester, UK, pp. 83–110 (2014)
5. W.H. Meiklejohn and C.P. Bean, *Phys. Rev.* 102, 1413 (1956).
6. W.H. Meiklejohn and C.P. Bean, *Phys. Rev.* 105, 904 (1957).
7. M.D. Hossain, R.A. Mayanovic, R. Sakidja, and M. Benamara, *J. Mater. Res.* 32, 269 (2017).
8. S. Dey, M.D. Hossain, R.A. Mayanovic, R. Wirth, and R. Gordon, *J. Mater. Sci.* 52, 2066 (2017).
9. M. d. Hossain, S. Dey, R.A. Mayanovic, and M. Benamara, *MRS Adv. FirstView*, 1 (2016).
10. L. Del Bianco, F. Boscherini, A.L. Fiorini, M. Tamisari, F. Spizzo, M.V. Antisari, and E. Piscopiello, *Phys. Rev. B* 77, 094408 (2008).
11. H.-C. Hsu, C.-C. Lo, and Y.-C. Tseng, *J. Appl. Phys.* 111, 063919 (2012).
12. A.C. Johnston-Peck, J. Wang, and J.B. Tracy, *ACS Nano* 3, 1077 (2009).
13. M. Patange, S. Biswas, A.K. Yadav, S.N. Jha, and D. Bhattacharyya, *Phys. Chem. Chem. Phys.* 17, 32398 (2015).
14. N. Rinaldi-Montes, P. Gorria, D. Martínez-Blanco, Z. Amghouz, A.B. Fuertes, L.F. Barquín, I. de Pedro, L. Olivi, and J.A. Blanco, *J. Mater. Chem. C* 3, 5674 (2015).
15. C.L. Yuan, *J. Phys. Chem. C* 114, 2124 (2010).
16. E. Skoropata, R.D. Desautels, C.-C. Chi, H. Ouyang, J.W. Freeland, and J. van Lierop, *Phys. Rev. B* 89, 024410 (2014).
17. N. Bayal and P. Jeevanandam, *J. Nanoparticle Res.* 15, 2066 (2013).

18. P.M. Ponnusamy, S. Agilan, N. Muthukumarasamy, M. Raja, and D. Velauthapillai, *J. Mater. Sci. Mater. Electron.* 27, 399 (2016).
19. M. El-Kemary, N. Nagy, and I. El-Mehasseb, *Mater. Sci. Semicond. Process.* (2013).
20. S. Hasan, R.A. Mayanovic, and M. Benamara, *MRS Advances First View*, 1 (2017).
21. A.I. Liechtenstein, V.I. Anisimov, and J. Zaanen, *Phys. Rev. B: Condens. Matter Mater. Phys.* 52(8), R5467 (1995)
22. H.J. Monkhorst and J.D. Pack, *Phys. Rev. B: Condens. Matter Mater. Phys.* 13(12), 5188 (1976)
23. J.P. Perdew, K. Burke, and M. Ernzerhof, *Phys. Rev. Lett.* 77, 3865 (1996)
24. R.D. Shannon, *Acta Crystallogr. Sect. A* 32, 751 (1976)
25. H. Khurshid, S. Chandra, W. Li, M.H. Phan, G.C. Hadjipanayis, P. Mukherjee, and H. Srikanth, *J. Appl. Phys.* 113, 17B508 (2013)

CHAPTER 4: SUMMARY

In my thesis project, I studied manganese and cobalt incorporated nickel oxide CSNs. The size of the $\text{NiO@Ni}_x\text{Mn}_{1-x}\text{O}$ and $\text{NiO@Ni}_x\text{Co}_{1-x}\text{O}$ CSNs was determined from XRD and TEM analyses to be ~ 24 and 30 nm, with an average shell thickness of ~ 2 and ~ 4 nm, respectively. EDS analyses confirm the presence of Mn and Co in the $\text{NiO@Ni}_x\text{Mn}_{1-x}\text{O}$ and $\text{NiO@Ni}_x\text{Co}_{1-x}\text{O}$ CSNs, respectively. The combined XRD and HR-TEM analysis provides evidence for the formation of core-shell nanostructure and confirms epitaxial growth of the shell over the core of the CSNs. Furthermore, the core-shell interface in both types of CSNs is found to be well ordered with minor amounts of structural defects, such as edge dislocations, stacking faults and cation vacancies. The structural defects are in part attributed to strain relaxation effects due to the lattice mismatch of the core vs the shell regions. The magnetic measurements using the SQUID and VSM showed that $\text{NiO@Ni}_x\text{Mn}_{1-x}\text{O}$ CSNs possess an AFM core and a FM/FiM shell: The magnetization data show significant coercivities and exchange bias fields at 5 K. The $\text{NiO@Ni}_x\text{Co}_{1-x}\text{O}$ CSNs were shown to also have an AFM core and a FM/FiM shell bimagnetic structure but exhibited weaker coercivity and exchange bias fields at 5 K.

A study of the dependence of the magnetic characteristics of $\text{NiO@Ni}_x\text{Mn}_{1-x}\text{O}$ CSNs on Mn concentration x was also performed. Although not quantified, upon increase in Mn concentration, the HR-TEM images showed evidence of a greater extent of structural defects and misfit dislocations in the interface/shell region of the $\text{NiO@Ni}_x\text{Mn}_{1-x}\text{O}$ CSNs. The magnetic measurements revealed that increasing Mn

concentration results in a significant increase in coercivity value from ~ 425 Oe to ~ 4787 Oe, accompanied by an increase in exchange bias (horizontal) value from ~ 130 Oe to 1729 Oe, at $5-10$ K in $\text{NiO}@\text{Ni}_x\text{Mn}_{1-x}\text{O}$ CSNs. The temperature-dependent magnetic characterization of 0.08M precursor concentration used to synthesize the $\text{NiO}@\text{Ni}_x\text{Mn}_{1-x}\text{O}$ CSNs showed retention of FM/FiM characteristics starting from 5K until room temperature (with a coercivity ~ 59 Oe and horizontal exchange bias ~ 16 Oe in FC measurement at 300K). Therefore, I was successfully able to synthesize for the first time inverted bimagnetic $\text{NiO}@\text{Ni}_x\text{M}_{1-x}\text{O}$ CSNs (M: Mn, Co), that is having the AFM@FM/FiM magnetic structure, using the hydrothermal nanophase epitaxy method. Furthermore, I have shown that it is possible to obtain room temperature FM/FiM behavior and an exchange bias effect from $\text{NiO}@\text{Ni}_x\text{Mn}_{1-x}\text{O}$ CSNs. This is attributed to the high Néel temperature point of the NiO core of the CSNs.

My DFT based ab-initio calculations shows that Mn/Co introduction in NiO and formation of $\text{Ni}_x\text{Mn}_{1-x}\text{O}/\text{Ni}_x\text{Co}_{1-x}\text{O}$ results in AFM coupling consistent with the magnetic structure of NiO, which in turn gives rise to strong/weak FiM properties due to an imbalance in Mn/Co and Ni individual magnetic moments, respectively. In addition, the introduction of the impurity cation creates impurity energy levels approximately midway within the bandgap. Furthermore, the DFT based calculations show that the bandgap is reduced to approximately 2.5 and 2 eV in $\text{Ni}_{0.88}\text{Mn}_{0.12}\text{O}$ and $\text{Ni}_{0.88}\text{Co}_{0.12}\text{O}$, respectively.

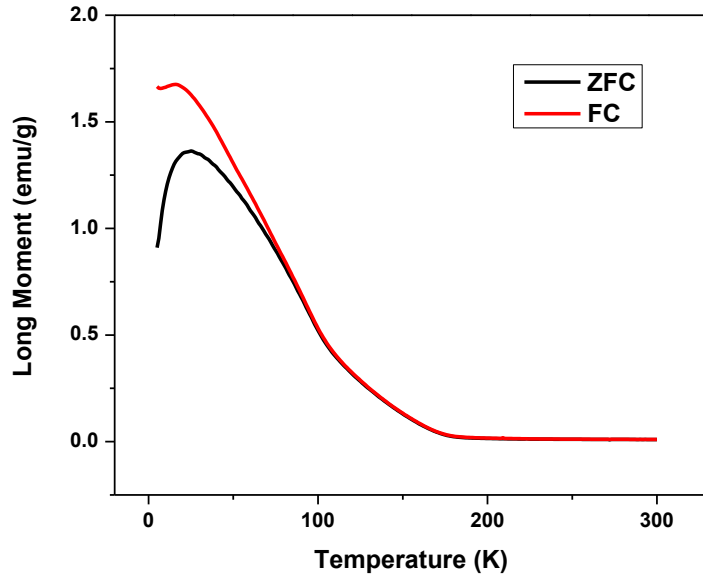
REFERENCES

1. A. López-Ortega, M. Estrader, G. Salazar-Alvarez, A.G. Roca, and J. Nogués, *Phys. Rep.* **1** (2014).
2. J. Mejía-lópez, A.H. Romero, and M.E. Garcia, *Materials* (2000).
3. Silva, É. Silva-Freitas, and J. Carvalho, *Adv. Appl. Biotechnol.* **237** (2012).
4. López-Ortega, A., Estrader, M., Salazar-Alvarez, G., Roca, A. G. & Nogués, J. *Phys. Rep.* **553**, 1–32 (2015).
5. M. B. Gawande, A. Goswami, T. Asefa, H. Guo, A. V. Biradar, D.-L. Peng, R. Zboril, and R.S. Varma, *Chem. Soc. Rev.* **44**, 7540 (2015).
6. J. Nogués, J. Sort, V. Langlais, V. Skumryev, S. Suriñach, J.S. Muñoz, M.D. Baró, *Phys. Rep.* **422.65** (2005).
7. W. Liu, W. Zhong, Y.W. Du, *J. Nanosci. Nanotechnol.* **8**, 2781 (2008).
8. A. López-Ortega, D. Tobia, E. Winkler, I. V. Golosovsky, G. Salazar-Alvarez, S. Estradé, M. Estrader, J. Sort, M.A. González, S. Suriñach, J. Arbiol, F. Peiró, R.D. Zysler, M.D. Baró, J. Nogués, *J. Am. Chem. Soc.* **132**, 9398 (2010).
9. D. W. Kavich, J. Dickerson, S. Mahajan, S. Hasan, J.H. Park, *Phys. Rev. B* **78**, 174414 (2008).
10. E. L. Winkler, E. Lima, D. Tobia, M.E. Saleta, H.E. Troiani, E. Agostinelli, D. Fiorani, R.D. Zysler, *Appl. Phys. Lett.* **101**, 252405 (2012).
11. N. Rinaldi-Montes, P. Gorria, D. Martínez-Blanco, A.B. Fuertes, L.F. Barquín, J.R. Fernández, I. de Pedro, M.L. Fdez-Gubieda, J. Alonso, L. Olivi, G. Aquilanti, I. Puente-Orench, and J.A. Blanco, *J. Phys. Conf. Ser.* **663**, 12001 (2015).
12. Iglesias, Oscar, Amilcar Labarta, and Xavier Batlle, *Journal of nanoscience and nanotechnology* **8.6**: 2761-2780 (2008).
13. Meiklejohn, W. H. & Bean, C. P. New Magnetic Anisotropy. *Phys. Rev.* **102**, 1413–1414 (1956).
14. M. Kiwi, *J. Magn. Magn. Mater.* **234**, 584 (2001).
15. Phan, Manh-Huong, et al. "Exchange Bias Effects in Iron Oxide-Based Nanoparticle Systems." *Nanomaterials* **6.11.221** (2016).

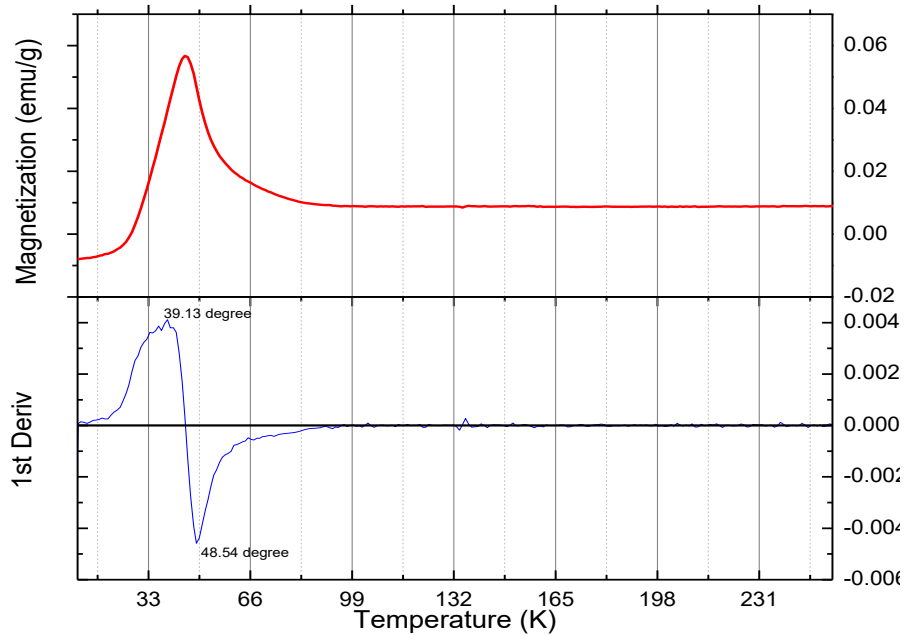
16. A. Roy, R. Gupta, and A. Garg, *Adv. Condens. Matter Phys.* **2012**, (2012).
17. V. Skumryev, S. Stoyanov, Y. Zhang, G. Hadjipanayis, D. Givord, and J. Nogués, *Nature* **423**, 850 (2003).
18. B. Je yadevan, C. N. Chinnasamy, O. Perales-Perez, Y. Iw asaki, A. Hobo, K. Shinoda, K. T ohji, and A. Kasuya, *IEEE Trans. Magn.* **38**, 2595 (2002).
19. H.-M. Lin, C. M. Hsu, Y. D.Y ao, Y. Y . Chen, T. T . K uan, F. A. Yang, and C. Y. Tung, *Nanostr. Mater.* **6**, 977 (1995).
20. L. Del Bianco, D. Fiorani, A.M.T esta, E. Bonetti, L. Sa vini, and S. Signoretti, *Phys. Rev. B* **66**, 174418 (2002).
21. D. Fiorani, L.Del Bianco, A.M.T esta, and K.N.T rohidou, *Phys. Rev. B* **73**, 092403 (2006).
22. R. K. Zheng, H.Liu, Y.W ang, and X.X.Zhang, *Appl. Phys. Lett.* **84**, 702 (2004).
23. O. Masala, D.Hof fman, N.Sundaram, K.P age, T.Prof fen, G.La wes, and R.Seshadri, *Solid State Sciences* **8**, 1015 (2006).
24. S. Gangopadhyay , Y.Y ang, G.C.Hadjipanayis, V.P apaefthymiou, C.M.Sorensen, and K.J.Klab unde, *J. Appl. Phys.* **76**, 6319 (1994).
25. S. Kang, G.X.Miao, S.Shi, Z.Jia, D.E.Nikles, and J.W .Harrell, *J. Am. Chem. Soc.* **128**, 1042 (2006).
26. M. Tadic, D. Nikolic, M. Panjan, and G.R. Blake, *J. Alloys Compd.* **647**, 1061 (2015).
27. M. D. Hossain, R.A. Mayanovic, R. Sakidja, and M. Benamara, *J. Mater. Res.* **32**, 269 (2017).
28. S. Dey, M.D. Hossain, R.A. Mayanovic, R. Wirth, and R. Gordon, *J. Mater. Sci.* **52**, 2066 (2017).
29. M. d. Hossain, S. Dey, R.A. Mayanovic, and M. Benamara, *MRS Adv. FirstView*, **1** (2016).
30. L. Del Bianco, F. Boscherini, A.L. Fiorini, M. Tamisari, F. Spizzo, M.V. Antisari, and E. Piscopiello, *Phys. Rev. B* **77**, 094408 (2008).
31. H.-C. Hsu, C.-C. Lo, and Y.-C. Tseng, *J. Appl. Phys.* **111**, 063919 (2012).
32. A.C. Johnston-Peck, J. Wang, and J.B. Tracy, *ACS Nano* **3**, 1077 (2009).

33. M. Patange, S. Biswas, A.K. Yadav, S.N. Jha, and D. Bhattacharyya, *Phys. Chem. Chem. Phys.* 17, 32398 (2015).
34. N. Rinaldi-Montes, P. Gorria, D. Martínez-Blanco, Z. Amghouz, A.B. Fuertes, L.F. Barquín, I. de Pedro, L. Olivi, and J.A. Blanco, *J. Mater. Chem. C* 3, 5674 (2015).
35. C. L. Yuan, *J. Phys. Chem. C* 114, 2124 (2010).
36. S. Hasan, R.A. Mayanovic, and M. Benamara, *MRS Advances First View*, 1 (2017).

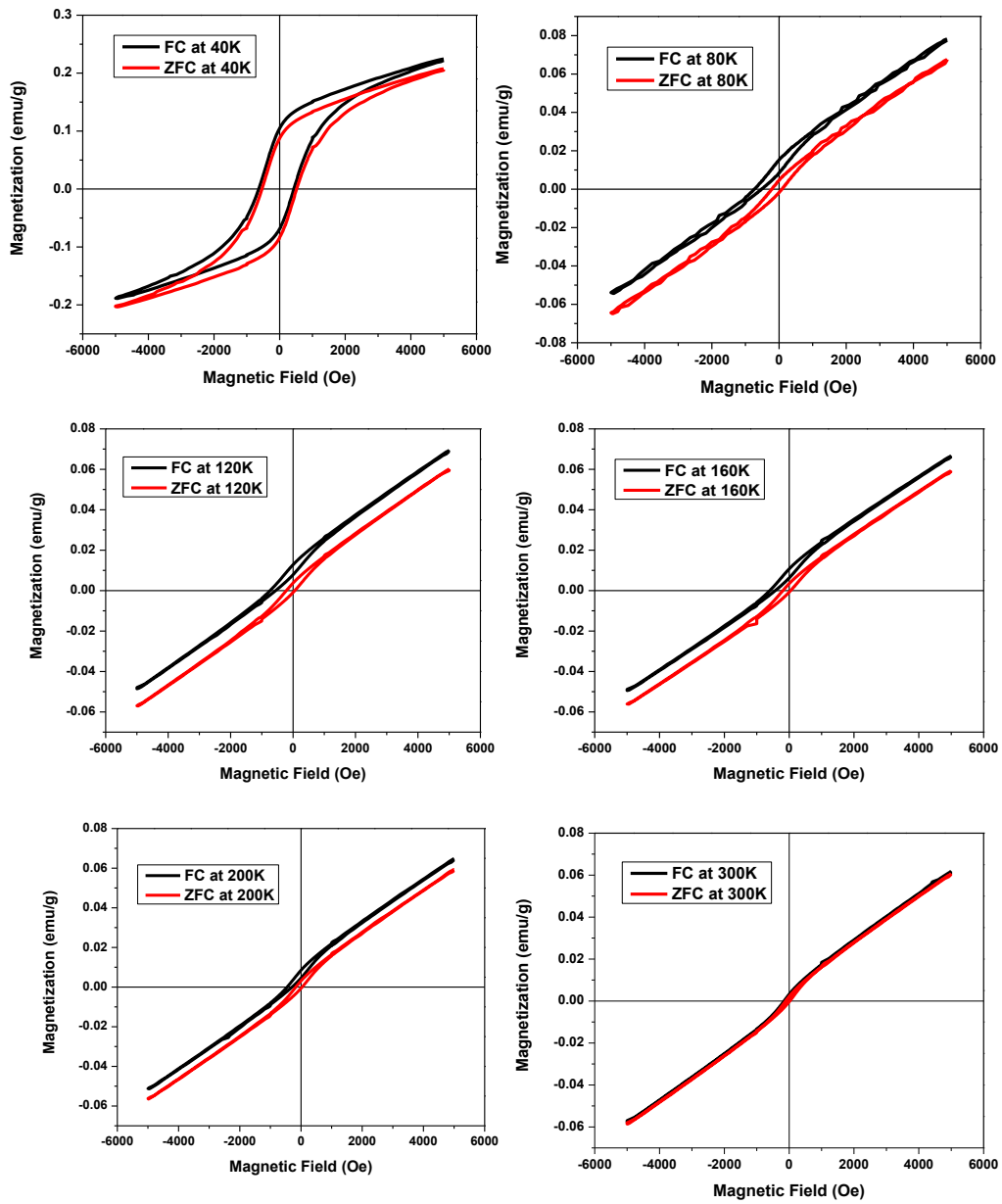
APPENDIX: ADDITIONAL DATA



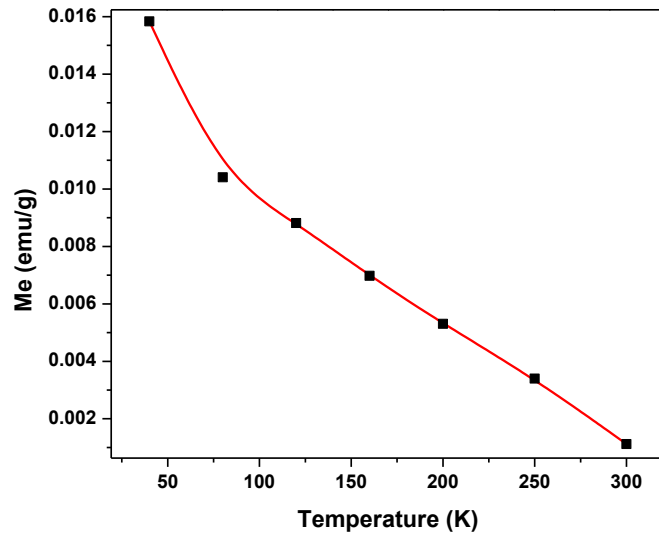
A.1: M vs T for 2nd batch of Manganese introduced CSNs



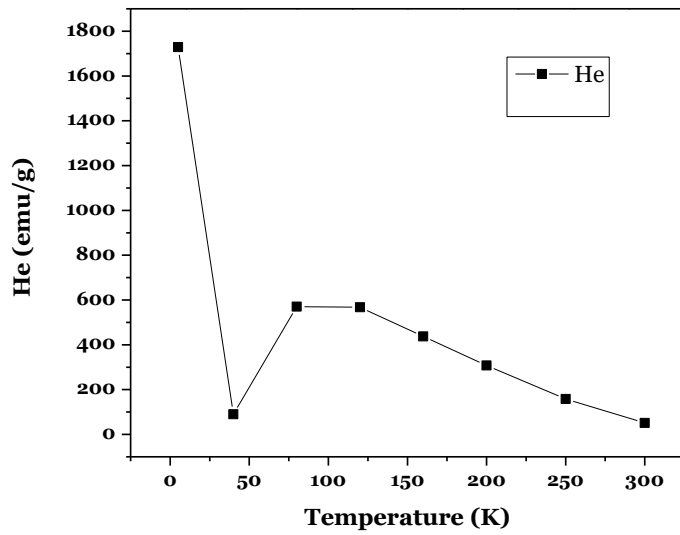
A.2: 1st order derivative of M vs T for 2nd batch of Manganese introduced CSNs



A.3: 1st order derivative of M vs T for 2nd batch of Manganese introduced CSNs



A.4: Temperature dependence of vertical axis shift of hysteresis in case of ZFC and FC



A.5: Temperature dependence of horizontal axis shift of hysteresis in case of ZFC and FC

A.5: Temperature-dependent magnetic parameters of sample 2 in NiO@Ni_xMn_{1-x}O

Temperature (K)	Coercivity (Oe)		H _{EB} (Oe)	M _{EB} (emu/gm)
	FC	ZFC		
5	4139.03	4786.90	1728.82	0.05531
40	537.05	529.11	89.72	0.01583
80	107.656	149.38	570.66	0.01041
120	89.72	131.91	567.77	0.00881
160	87.50	117.77	437.16	0.00698
200	80.91	106.04	307.45	0.00531
250	74.73	83.49	158.22	0.00341
300	63.49	62.69	51.10	0.00112